# The structure of the crust and uppermost mantle beneath South China from ambient noise and earthquake tomography

Longquan Zhou[1], Jiayi Xie[2], Weisen Shen[2], Yong Zheng[3], Yingjie Yang[4], Haixia Shi[1], and Michael H. Ritzwoller[2]

1. China Earthquake Network Center, Beijing, 100045, China (lqzhou@seis.ac.cn)

2. Center for Imaging the Earth's Interior, Department of Physics, University of Colorado at Boulder, Boulder, CO 80309 USA (michael.ritzwoller@colorado.edu)

3. Institute of Geodesy and Geophysics, CAS, Wuhan, China (zhengyong@whigg.ac.cn)

4. Department of Earth and Planetary Sciences, Macquarie University, 2109 Sydney Australia (yingjie.yang@mq.edu.au)

[1] Two years of continuous recordings of ambient seismic noise observed at 354 stations in South China from 2009 and 2010 are used to estimate Rayleigh wave group and phase velocity maps from 6 to 40 sec period. These results are merged with Rayleigh wave phase velocity maps from 25 to 70 sec period derived from earthquakes in the same time frame. Eikonal tomography generates the dispersion maps, which, by Monte-Carlo inversion, are used to estimate a 3-D Vsv model of the crust and upper mantle to a depth of 150 km across all of South China with attendant uncertainties. A clear image emerges of the "West Yangtze Block", a region of the western Yangtze Craton characterized by relatively thick crust (~40 km) overlying a seismic mantle lithosphere that extends to at least 150 km that may have been the nucleus of formation for the Yangtze craton in the Archean and presents a present-day obstacle to the eastward expansion of Tibet. The West Yangtze Block contrasts with the thinner crust (~30 km) and mantle lithosphere (~70-80 km) beneath the eastern Yangtze Craton and South China Foldbelt. These observed differences are consistent with models of flat-slab subduction in the Mesozoic (e.g., Li & Li, 2007) that may have eroded the lithosphere of the eastern Yangtze Craton and the South China Foldbelt.

## 1. Introduction

[2] The recent tectonic evolution of eastern Asia has been driven by subduction to the east and continental collision to the west. Eastern China is a fairly passive participant in this neo-tectonic framework, having formed no later than the early Paleozoic. The paleo-architecture of Eastern China is dominated by two crustal blocks, the Sino-Korean (or North China) Craton and the South China Block, which are separated by the Qinling-Dabie-Sulu orogenic belt. The South China Block is the subject of this study and is believed to have formed by the collision between the Yangtze Craton and the Cathasyia Block [*e.g., Zheng et al., 2006*]. The Cathasyia Block divides further into the South China Foldbelt and the younger Youjiang Block to the west [*Zhang et al., 2003*]. (See Figure 1a.) The Sino-Korean and Yangtze Cratons are both Archean in age, but the geological structure of the Yangtze Craton is more poorly understood because it is largely shrouded in Proterozoic cover strata. The Yangtze Craton encompasses two large sedimentary basins, the Jianghan Basin and the Sichuan Basin, which may have served as the nucleus of formation for the Yangtze Craton [*Zhang et al., 1984*]. The South China Block is tectonically stable and suffers few earthquakes, except along its northern margin and western margin where it presents an obstacle to eastern mass transport from the Tibetan Plateau [*e.g., Royden et al., 1997*] and numerous large earthquakes occur [*e.g., Zhang et al., 2003*].

[3] A number of factors have inhibited the seismic imaging of the crust and upper mantle beneath the South China Block, including the lack of seismicity and poor

station coverage historically. At least parts of the South China Block have been imaged by larger scale tomographic studies, including *Ritzwoller and Levshin [1998], Ritzwoller et al. [1998], Teng et al.* [2001], *Villasenor et al. [2001], Lebedev and Nolet [2003]*, *Huang et al.* [2003], and *Zheng et al. [2008].* By the end of 2007, however, a new digital seismic observing system was completed in China based on aggregating seismic stations from individual provincial networks [*Zheng et al., 2010a*]. We refer to this as CEArray. This data resource has already been used for P-wave travel time tomography [e.g., *Li and van der Hilst, 2010*] and surface wave tomography in neighboring regions [*e.g., Yang et al., 2010, 2011; Zheng et al., 2010b, 2011*]. CEArray in South China consists of 425 seismic stations equipped with very broadband (VBB), ultra broadband (UBB), or broadband (BB) seismometers (Figure 1b).

[4] We present here a new step in imaging the crust and uppermost mantle beneath the South China Block: Rayleigh wave tomography in South China extending from periods of 6 sec to 70 sec based on ambient noise and earthquake tomography and construction of a 3D Vsv model of the crust and uppermost mantle to a depth of 150 km. Ambient noise has been shown to be strong across China (e.g., *Yang and Ritzwoller, 2008b*) and ambient noise tomography is performed from 6 to 40 sec period. Earthquake tomography is performed from 25 to 70 sec period across the study region. In the period band of overlap (25 – 40 sec) we average the phase velocity maps from ambient noise and earthquakes, weighting up the ambient noise maps at the short period end and earthquake maps at the long period end. The eikonal

tomography method (*Lin et al., 2009*) is used to produce the Rayleigh phase speed maps using both ambient noise and earthquake data. Eikonal tomography is a ray theoretic method but it models rays bent by lateral variations in structure and produces meaningful uncertainty estimates in the resulting dispersion maps. For the ambient noise, we demonstrate consistency for the phase velocity maps derived using eikonal tomography and the straight ray tomography method of *Barmin et al. (2001)* also produce group velocity maps based on the method of Barmin et al. We also demonstrate consistency between the phase velocity maps produced from ambient noise and earthquakes in the period band of their overlap.

[5] Because a large number of disparate agencies in China are responsible for operating and maintaining the provincial seismic networks that compose CEArray, to combine data from all of these networks across the region of study requires careful quality control. The procedures that we have developed to insure the quality of the phase (i.e., travel time) response of the vertical component of the CEArray stations are described in section 2.1. After discarding 71 of the original 425 stations, we find that the resulting data set is of very high quality. The fraction of stations with problems on the vertical component (~9%) is much lower than that uncovered by an analysis of horizontal components of a larger set of CEArray stations by Niu and Li (2011) who found that about one third of the stations have some sort of problem, including misorientation of the two horizontal components, mislabeling, and polarity reversals in one or more of the components.

The goal of this study and related papers of *Zheng et al. (2010b, 2011)* and *Yang et*

*al. (2010, 2011)* is to make significant strides toward developing an integrated, highly resolved shear wave speed (Vs) model of the crust and uppermost mantle beneath all of China. *Zheng et al. (2011)* focus on northeast China and *Yang et al. (2010, 2011)* on Tibet. The complementary focus of the current paper is southeast China and this paper also applies earthquake data to extend the dispersion maps to longer periods. The purpose of this paper is to establish the quality of the surface wave data in South China, present the broad-band dispersion maps that result from ambient noise and earthquake data, demonstrate their consistency and robustness, and present a preliminary 3D Vsv model of the crust and uppermost mantle. The resolution of structures that emerges in South China is unprecedented.

## 2. Data and Methods

### 2.1 Data quality control

The primary means to assess and control the quality of the data is by measuring the consistency between the Rayleigh wave phase travel times observed between different stations using ambient noise. The measurement of Rayleigh wave group and phase travel times between stations is described in section 2.2. Consistency is determined from the ability of smooth phase speed maps (such as those shown later in Fig. 9) to fit the measured travel times. For each station at a given period, we compute the difference between the observed travel time to every other station and the travel time to that station predicted by the phase velocity map at that period. This is an iterative process; as stations are discarded the phase velocity maps are updated and the process re-initiates.

An example at 20 sec period is shown for a station judged to be acceptable (CQSHZ) in Figure 2. The histogram in Figure 2a is quite narrow, although there are a few outliers that turn out to be caused by other problematic stations (not CQSHZ). Observed minus predicted travel times to the other stations are plotted in Figure 2b at each of the other station locations, identifying the locations of the large misfits with darker colored reds or blues. The standard deviation of misfit for good central stations is typically near to or less than 2 sec. The average misfit relative to this station is about -0.2 sec, meaning that the observed travel times are on average less than the predicted travel times, or the observed waves are slightly faster than predicted. However, if the average is taken within 1 standard deviation of the mean, the average misfit is of much smaller amplitude, -0.05 sec, implying that the overall average is perturbed from zero largely by other stations with instrumental problems.

The result shown in Figure 2 is for a station that is retained for further analysis. There are more problematic stations, however, and several examples at 20 sec period are shown in Figure 3. Figure 3a,b illustrates a station (HNJIS) that is mis-located by about 1.5 km. This is revealed by the dipolar misfit pattern observed in Figure 3b. Using this method, 9 stations are determined to be mis-located, and these stations are identified in Figure 1b with blue triangles. In principle, we could re-locate these stations using the misfit data, but we simply discard them because they are few in number and not concentrated in one area. An unknown, perhaps time variable, instrument response error is revealed in Figure 3c,d for station SNLOXT. There are 13 of these stations that are identified in Figure 1b with black triangles. These stations

are also discarded even though several are clustered in Shaanxi province, because we do not know how to correct them. A better understood $\pi$ (10 sec) instrument response error is illustrated in Figure 3e,f, which is diagnostic of a polarity error. The bi-modal misfit pattern seen in Figure 3e scales with period. However, this problem also does not seem to be rectifiable. When we correct the apparent polarity error the resulting waveforms still disagree with waveforms observed at nearby stations, implying that the $\pi$-misfit reflect a more profound error. Thus, we also discard the 11 stations in this category that are identified in Figure 1b with red triangles, most of which reside in Guangdong Province. The resulting list of 33 problematic stations is presented in Table 1. We also do not have response files for 38 additional stations.

Removal of the 33 problematic stations and the 38 stations for which we lack response files results in a set of 354 stations where we possess response files that are determined to be of good quality. These are the stations that are used for both ambient noise and earthquake tomography in southeast China. Based on these stations alone, Figure 4 presents the phase travel time misfits at periods of 8, 14, 20, and 30 sec from ambient noise, again comparing the observed inter-station travel times to those predicted from dispersion maps such as those plotted in Figure 9. Rayleigh wave phase travel time misfits average about 1 sec below 30 sec period, which is a quality statistic consistent with results using USArray (e.g., *Lin et al., 2008*). As Figure 5 shows, group travel time misfts are higher because group velocity is a more difficult measurement than phase velocity. A factor of 3 ratio between the misfit for group and phase times is commonly observed.

## 2.2 Ambient noise data processing

[4] The use of ambient noise to extract surface wave empirical Green's functions (EGFs) and to infer Rayleigh wave [e.g., *Sabra et al.*, 2005; *Shapiro et al.*, 2005] group and phase speeds in continental areas is well established [e.g., *Bensen et al., 2007*; *Lin et al., 2008*]. The resolution of ambient noise tomography is limited primarily by the number, distribution, and quality of stations. Southeast China possesses a large number of well-distributed stations that, after quality control procedures have been applied, yields a data set of very high quality. It is, therefore, an ideal location for ambient noise tomography. We process two years of continuous vertical component ambient noise observed at 354 seismic stations in South China, so the cross-correlations predominantly contain only Rayleigh waves.

[5] The data processing procedures we adopt here follow those of *Bensen et al.* [2007] and *Lin et al. [2008]*. Continuous data are decimated to one sample per sec and are then filtered in the period band from 5 to 50 sec. Instrument responses are then removed from the continuous data because different types of seismic sensors are used; most are BB (long period corner at 20 sec) but some are VBB (120 sec corner) or UBB (360 sec corner). Accurate surface wave dispersion measurements can be obtained at periods well above the corner period of the instrument. Time-domain normalization in a running window 80 seconds in length is applied to suppress the influence of earthquake signals and other irregularities and spectral whitening is applied to flatten spectra over the entire period band (5-50 sec). After completing these processing steps, cross-correlations are performed daily between pairs of

stations in the period band from 5-50 sec and then are stacked over the two-year time window.

[6] Figure 6 displays an example cross-correlation record section between Chinese station AHJIX and other stations in South China. Strong surface wave signals are observed on both positive and negative correlation lags. To simplify data analysis and enhance the signal-to-noise ratio (SNR) of the surface waves, we separate each cross correlation into positive and negative lag components and then add the two components to form the so-called "symmetric component."

[7] Group and phase velocity dispersion measurements of Rayleigh waves are obtained from the symmetric components of inter-station cross-correlations by automatic frequency-time analysis (FTAN) [*Bensen et al.*, 2007]. Group velocity is measured on the envelope of the surface wave packet and phase velocity measurements are made on the phase content of the wave packet. Group and phase velocity are not constrained to agree even though they are related theoretically [e.g., *Levshin et al., 1999*]. The automated FTAN dispersion measurements are winnowed by applying three criteria to select reliable measurements for surface wave tomography. (1) The distance between two stations must be greater than three wavelengths for group velocity and two wavelengths for phase velocity to ensure sufficient separation of the surface wave packets from precursory noise. (2) SNR must be greater than 15 at each period for the measurement at that period to be accepted. (3) As described in section 2.1, we require that the measurements agree with one another across the data set. Measurements that can be fit well by a smoothed tomographic

map are considered to cohere within the data set as a whole. Based on this analysis, 33 stations are rejected, as discussed in section 2.1, yielding 354 stations judged to have acceptable response files. In addition, at each period we discard all measurements that are misfit by the phase velocity map at that period by more than half a period. This effectively removes $2\pi$ phase errors. Resulting misfit statistics are listed in Table 2.

[8] In principle, 354 stations would produce up to about 63,000 cross-correlations. The smaller numbers presented in Table 2, ranging up to about ~50,000 paths between 12 and 20 sec period, principally reflects the strength of ambient noise in China, which reduces above ~25 sec period. Still, even at 40 sec period more than 12,000 paths remain. Also, at periods below ~10 sec, scattering from small-scale heterogeneities makes measurement of surface wave speeds more difficult. Phase velocity measurements generally outnumber group velocity measurements because of differences in the inter-station distance data selection criterion.

[9] We perform surface wave tomography on the selected dispersion measurements to produce Rayleigh wave group and phase velocity maps on a 0.5° x 0.5° grid using the straight ray tomography method of *Barmin et al.* [2001] as well as eikonal tomography, which models ray bending due to lateral heterogeneities (*Lin et al.,* 2009). A comparison between the results of these two methods is presented in Figure 7 for the 20 sec Rayleigh wave phase velocity. The results are quite similar; in particular, the mean across each map differs only by 0.2 m/s. The similarity of the maps produced by these two methods results because the relatively short paths considered here are not strongly affected by off-great circle effects at this period [e.g.,

*Lin et al., 2009*]. At shorter periods (e.g, 10 sec) near the Sichuan Basin, differences are somewhat stronger, however. Because eikonal tomography produces uncertainty estimates for the maps, we present the results here using that method for phase velocities (Figure 9a-d). However, the eikonal equation governs propagation of phase not group times; thus, for group velocities we use the straight-ray tomography method of Barmin et al. (2001) with confidence given the similarity of the methods evidenced in Figure 7. We ignore finite frequency effects here, but they are weak in the period band in which ambient noise is applied here [e.g., *Lin et al., 2011; Ritzwoller et al., 2011*].

Rayleigh wave group velocity maps from ambient noise data are presented in Figure 8 at periods of 8, 14, 20, and 30 sec. Similarly, the phase velocity maps are presented in Figures 9a-c and 10a. We examine the maps in subsequent sections, after discussing earthquake data processing which is applied at periods greater than 25 sec.

[10] Misfit statistics for the final tomographic maps provide information about the quality of the dispersion measurements. Below 30 sec period, in the primary pass-band of Chinese BB instruments, phase travel time misfit is about 1 second and group travel time misfit is several times larger, the typical relationship between phase and group travel time misfits. Misfit degrades below 10 sec due to scattering from small-scale heterogeneities that makes group and phase velocity measurements more difficult and also because it is more difficult to resolve $2\pi$ phase ambiguities. Misfit also increases above 30 sec period because of reduction in the level of ambient noise, roll off of many of the instruments, and because paths are typically longer, on average.

Overall, misfit statistics establish that data quality is very high, particularly between 10 and 30 sec period where it is similar to misfits derived from USArray data in the US [e.g., *Lin et al., 2008*].

## 2.3 Earthquake data processing

We apply the eikonal tomography method described by Lin et al. (2009) to earthquake data to determine Rayleigh wave phase speed maps from 25 sec to 70 sec period. Earthquake waveforms are accumulated following all events with surface wave magnitudes larger than 5.0 that occurred in the years 2009 and 2010. This yielded a set of 595 earthquakes closer than 15,000 km from the center of the array. Phase travel times are tracked across the array following each earthquake for all stations where SNR is greater 10 at a given period and the $2\pi$ phase ambiguity is resolved. Unless SNR>10 at a given period for >50 stations, the earthquake is discarded for that period. This results in about 500 earthquakes at 25 sec period and diminishes to about 300 earthquakes at 70 sec period. Finite frequency effects are ignored in the eikonal tomography method, although ray bending due to lateral structural variations is modeled. We have obtained maps to periods >70 sec, but to use them finite frequency effects should be modeled (*Lin and Ritzwoller, 2011*).

The earthquake based Rayleigh wave phase velocity map at 32 sec period is compared with the map derived from ambient noise in Figure 10. Generally, there is good agreement. The lateral variation of the difference between ambient noise and earthquake maps (Fig. 10d) is similar to differences between ray theories (Fig. 7d). The earthquake-derived map is faster by an average of about 12 m/s (0.3%). Much of

this difference is near the edge of the map, however. The agreement in the distribution and amplitude of the anomalies is typical for comparisons between ambient noise and earthquake-derived maps (e.g., *Yang and Ritzwoller, 2008a; Ritzwoller et al., 2011*), and the disparity in the mean of the maps is also similar to what is observed using USArray in North America (Yang and Ritzwoller, 2008).

## 3. Dispersion Maps

[11] Rayleigh wave group and phase velocity maps are produced on a 2 sec period grid from 6 sec to 20 sec period and then on a 5 sec period grid to 70 sec period. Ambient noise maps extend up to 40 sec period and earthquake derived maps from 25 sec to 70 sec period.

Examples of these maps from ambient noise at 8, 14, 20 and either 30 sec or 32 period are shown in Figures 8, 9a-c, 10a. Velocity perturbations are plotted only where resolution is better than 100 km, where resolution is defined as twice the standard deviation of a 2-D Gaussian fit to the resolution surface at each geographic node [*Barmin et al. 2001*]. At each period, the group velocity anomalies are sensitive to shallower structures than the phase velocities. Thus, for example, phase velocity maps should be compared with shorter period group velocity maps. Earthquake-derived phase velocity maps at 32, 40, 50, and 70 sec period are shown in Figure 9d-f and Figure 10b..

The method of eikonal tomography provides uncertainties in the dispersion maps. Examples at periods of 20 sec and 40 sec are presented in Figure 11, where the shorter period result is from ambient noise and the longer period result derives from

earthquakes. Except near map boundaries, the uncertainties are largely spatially invariant. The average uncertainty at 20 sec is 10 m/s and at 40 sec is 18 m/s, and uncertainties typically grow near the edges of the maps. Uncertainties determined from ambient noise by eikonal tomography are generally underestimated (e.g., *Lin et al., 2009*). For this reason we double the uncertainties from ambient noise, which brings them into better agreement with the uncertainties from earthquakes. We also ensure that uncertainties are not less than 10 m/s at any period or location. Realistic uncertainties result, similar to those presented for ambient noise across the western US by *Lin et al. (2009)*.

[12] The short period maps, e.g., 8 and 14 sec group velocity and 8 sec phase velocity, are strongly influenced by the shallow part of the crust, particularly the existence of sediments. The major sedimentary basins, such as the Sichuan Basin, Jianghan basin, the North China Plain, North Jiangsu Basin, and the South China Sea between the mainland and Hainan Island, all appear as low velocities. The boundary between the South China Block and the North China Platform is clear because of sediments deposited near the boundary of these regions. The 14 sec group velocity map (Fig. 8b) also shows a clear distinction between the South China Foldbelt and the generally faster Yangtze Craton. At short periods, the Youjian Block is not distinguishable from the South China Fold Belt.

[13] At intermediate periods, 20 sec − 32 sec, the maps are affected by mid- to lower-crustal shear wave speeds and crustal thickness. At these periods, the velocity features lose the geological coherence seen at shorter periods; the predominant

structure is a west to east velocity variation. For example, the 30 sec group velocity and the 20 sec phase velocity maps are quite similar. The Yangtze Craton is roughly bifurcated on these maps, being slow in the west and fast in the east, reflecting thicker crust in the west [*Zhang et al.*, 1984; *Teng et al.*, 2003]. At these periods, the Youjian Block is distinguishable from the South China Foldbelt, perhaps because of the influence of active tectonics driven by the expansion of Tibet in the western part of the study region. However, the eastern Yangtze Craton and South China Foldbelt are not distinguishable, consistent with the expectations or results of earlier studies [*Li and Mooney*, 1998; *Huang et al.* 2003].

[14] The deepest sensitivity of these maps is provided by the longest period maps (e.g., 40-70 sec phase velocity maps in Fig. 9d-f). The 32 sec phase velocity maps remain strongly sensitive to crustal thickness where thicker crust appears as lower velocities. The 40 sec map also is sensitive to crustal thickness, but reflects upper mantle shear wave speeds more strongly. This difference in sensitivity accounts for differences between the 32 sec and 40 sec maps. Very low phase velocities are imaged for the Bayan Har, Chuandian, and South Yunnan Blocks. This is expected for these actively deforming regions with thicker crust. A prominent high velocity anomaly appears on the 50 – 70 sec maps in the western Yangtze Craton reflective of high wave speeds in the upper mantle and thick mantle lithosphere. This and other features of the resulting model are discussed further in section 5.

**4. Construction of the 3D Vsv model**

This study is based exclusively on Rayleigh waves, which are sensitive to vertically polarized shear wave speeds (Vsv) that may be slower than horizontally polarized shear speeds (Vsh) in regions where anisotropic minerals are preferentially aligned in the horizontal plane. The velocity difference between Vsv and Vsh is referred to as radial anisotropy. Thus, the model we produce is a Vsv model. In the presence of substantial radial anisotropy, Vsv can be several percent lower than the effective isotropic shear wave speed, Vs. Radial anisotropy is common in both the mantle (e.g., *Ekstrom and Dziewonski, 1997; Shapiro and Ritzwoller, 2002*) and the crust (e.g., *Shapiro et al., 2004; Moschetti et al., 2010a,b*), and is geographically variable. We will generally refer to our 3D model as being a Vsv model, but for simplicity will also refer to it as shear wave speed or Vs model.

The 3D Vsv model is estimated using the Rayleigh wave phase and group velocity maps from 6 to 70 sec period with attendant uncertainties on a 0.5°x0.5° grid across the study region. Local dispersion curves from the four locations identified with diamonds in Figure 1a are shown in Figure 12 with error bars. The error bars are period dependent and for Rayleigh wave phase velocity represent one standard deviation uncertainties determined by eikonal tomography at each period, as discussed in section 3. Group velocity maps are not determined with eikonal tomography, thus they result entirely from ambient noise (not earthquakes) using the method of *Barmin et al. (2001)* up through 40 sec period.

The ambient noise and earthquake-derived maps are merged in the period band of overlap of the methods, between periods of 25 sec and 40 sec. The ambient noise and earthquake-derived maps are weighted up at the short and long period ends of this range, respectively. The ambient noise and earthquake-derived uncertainties result from the same weighting scheme applied to the individual dispersion maps. The group velocity uncertainty is twice the phase velocity uncertainty at each period.

The 3D model is constructed via a Monte-Carlo method that is similar to the methods of *Shapiro and Ritzwoller (2002)* and *Yang et al. (2008)* but is more closely related to the method of *Shen et al. (2011).* Details can be found in *Shen et al. (2011),* which we summarize briefly here.

Starting from the global Vsv model of *Shapiro and Ritzwoller (2002),* uniformly distributed perturbations in Vsv are considered using a single sedimentary layer with variable thickness and shear velocity, four B-splines for Vsv in the crystalline crust, and five B-splines in the mantle to a depth of 200 km, below which the model is a constant velocity half-space. The resulting model is vertically smooth in both the crystalline crust and mantle. Moho depth is allowed to vary in a uniform interval of $\pm 10$ km relative to the starting model. Vsv is constrained to increase monotonically in the crust and the depth derivative of velocity directly below Moho is constrained to be positive (i.e., velocity increases with depth right below Moho, but can decrease deeper into the mantle). Both constraints are introduced to reduce model space, in particular the magnitude of the trade-off between Moho depth and structures at depths adjacent to Moho. The model has no radial anisotropy, thus Vs = Vsh = Vsv. Also, we

17

assume that the crystalline crust is a Poisson solid and set Vp = 1.73Vs, in the sediments we use Vp = 2.0Vs, and for density we use the scaling relation advocated by *Christensen and Mooney (1995)*: $\rho = 0.541 + 0.3601Vp$, where $\rho$ is in g/cm$^3$ and Vp is in km/s. We apply a physical dispersion correction (*Kanamori and Anderson, 1977*) using the Q model from PREM (*Dziewonski & Anderson 1981*), and the resulting model is reduced to 1 sec period.

Models are chosen randomly guided by a Metropolis algorithm (e.g., *Mosegaard and Tarantola, 1995*) and are judged to be acceptable if the reduced $\chi^2$ misfit to the dispersion curves is less than 0.5 units greater than the minimum misfit, $\chi^2_{min}$ at each location. Reduced $\chi^2$ misfit is defined as follows:

$$\chi^2 = \frac{1}{N}\sum_{i=1}^{N}\frac{(d_i - p_i)^2}{\sigma_i^2}$$

where $N$ is the total number of discrete dispersion measurements along the phase and group velocity curves, $d_i$ is one of the measurements with uncertainty $\sigma_i$, and $p_i$ is the predicted dispersion measurement (Rayleigh wave phase or group speed) for the considered model. RMS misfit (square root of reduced $\chi^2$) averages about 1.3 across the region of study, establishing both the plausibility of the uncertainty values and the ability of the dispersion curves to be fit by a vertically smooth Vsv model with the imposed constraints. Much of the misfit results from phase velocities above 40 sec period and group velocities from 20 to 40 sec period. Uncertainties in both appear to be slightly underestimated, but not at a level to affect the final model appreciably.

As examples, the procedure yields the four ensembles of models presented in Figure 13 for the four pairs of dispersion curves shown in Figure 12. The ensemble is represented by the grey shaded region, which presents two standard deviations around the mean at each depth in each direction. The dispersion curves predicted by the best-fitting model are shown in Figure 12 as the blue (group velocity) and red (phase velocity) lines. The RMS misfit listed on each of the panels of Figure 12 is the square root of the reduced $\chi^2$ value. At each depth, the Vsv model that we show here and its uncertainty is defined by the middle and quarter-width ($1\sigma$) of the ensemble at each depth, respectively. The uncertainties in the model are largest where shear wave speeds trade-off effectively with boundary topography, which occurs near free boundaries in the model: Moho and the base of the sedimentary layer. This is why uncertainties grow near the top of the crystalline crust and both above and below Moho.

Figure 14 shows the Vsv model at two depths in both the crust (10 km, 25 km) and the mantle (70, 140 km). Because the dispersion curves only extend to 70 sec period, the model is not reliable beyond a depth of ~150 km. Crustal thickness and uncertainty are shown in Figure 15 and uncertainties at the depths shown in Figure 14 are presented in Figure 16. Four vertical slices of the model are presented in Figure 17 on profiles along 30°N latitude, 110°E longitude, a diagonal profile extending from the northwest to southeast part of the study region, and 115°E longitude, identified with lines in Figure 14d. The model is discussed in detail in section 5.

Model uncertainties are shown in Figure 16 corresponding to the depth slices in Figure 14. At each depth, uncertainties tend to be bifurcated, being relatively constant and low over an extended region, but growing larger elsewhere. This bifurcation is caused by the elevation of uncertainties due to the trade-off between perturbations in shear velocity near a boundary and topography on that boundary. The closeness to a boundary changes over the region at each depth. For example, the trade-off between Vs at 10 km depth (Fig. 16a) with sediment thickness only occurs in sedimentary basins where sediments are thickest, namely in the northern Sichuan Basin. Uncertainties at 10 km depth exceed 150 m/s (>5%) below the Sichuan Basin whereas across most of South China they are less than 50 m/s (~1.5%). At 25 km depth (Fig. 16b), uncertainties are small where this depth is most distant from the Moho, which occurs where the crust is thickest, namely in the western part of the study region where uncertainties average about 50 m/s (~1.3%). However, in the eastern Yangtze Craton and South China Foldbelt, uncertainties are about twice as large on average (>3%). This is because 25 km depth is in the lower crust in these regions, relatively close to the Moho, and is in the middle crust in the western part of the study region. Uncertainties in Moho depth (Fig. 16c) are more uniform than the velocities but are somewhat larger in the western than the eastern parts of the study region. Thus, uncertainty in Moho depth is larger where crust is thicker, averaging about 4 km in the western Yangtze craton and about 3 km beneath the South China Foldbelt. At 70 km depth, uncertainty averages about 60 m/s across most of the study region, but grows to 2-3 times this value in Tibet. This is also a crustal thickness effect because the Moho

is deep enough beneath Tibet to trade-off with seismic velocities at 70 km. Uncertainties are higher at 140 km, generally more than 100 m/s, due to weaker constraints on structure at this depth.

## 5. Discussion

### 5.1 Structural features of the 3D model

Shear velocities in the shallow crust at 10 km depth are fairly homogeneous across most of the study region being about 3.48 km/sec across most of the eastern Yantgze craton and the South China Foldbelt. There are two primary exceptions. First, the principal velocity anomalies are the low wave speeds beneath the sedimentary basins, notably the Sichuan Basin, the Jianghan Basin, and offshore between Hainan Island and the mainland. The Sichuan and Jianghan basins may be seen more clearly in the vertical slices in Figure 17, profiles A-A', B-B'. The lowest wave speeds are observed beneath the northern Sichuan Basin. As discussed in the preceding section, shear wave speeds at depths near internal boundaries are not well determined. Sedimentary basins, in particular, do not have an entirely well defined lower boundary. Thus, exceptionally low velocities at 10 km depth beneath the basins may be caused by leakage from sediments at shallower levels. Second, the Tibetan crust at 10 km depth is also slow relative to the regional average, with a value (~3.35 km/s) that is consistent with the observation at 15 km depth by Yang et al. (2011). These low velocities are probably caused by to elevated upper crustal temperatures beneath Tibet. There is a third more subtle variation worthy of note: the eastern Yantgze craton is slightly faster at 10 km

depth (avg: ~3.55 km/s) than the South China Foldbelt (avg: ~3.48 km/s) and is seen more clearly on the 14 sec group velocity map shown in Figure 8b. This is reflective of differences in composition and thermal history between these two regions.

The deeper crust beneath the Sichuan Basin is quite fast, however, as can been seen in Figure 14b and Figure 17, profiles A-A', B-B'. The middle and lower crust beneath the Sichuan and Jianghan basins, therefore, are probably cold and rheologically stiff.

Deeper crustal shear wave speeds (e.g., Fig. 14b), Moho depth (e.g., Fig. 15a), and uppermost mantle shear wave speeds (e.g., Fig. 14c,d) are best considered together. Exclusive of Tibet, the region of study breaks into two major subdivisions.

(1) The western Yangtze craton is characterized by thick seismic lithosphere (>100 km), a crust mostly thicker than 40 km, but a relatively slow middle and lower crust (Fig. 14b) outside of the Sichuan Basin. The thick lithosphere can be seen clearly as high shear wave speeds on Figure 14c,d, which extend to the base of the vertical profiles A-A', B-B', C-C' seen Figure 17. For the purposes here, we define the thickness of the seismic lithosphere as the depth in the mantle where shear wave speed dips below 4.5 km/s. Essentially the entire western Yangtze craton is faster than 4.5 km/s at 70 km depth with wavespeeds underlying the Sichuan Basin reaching as high as $4.75 \pm 0.06$ km/s. We refer to the region with thick crust and mantle lithosphere beneath the western Yangtze craton as the "West Yangtze Block". High velocities beneath the center of the West Yangtze Block extend to at least 150 km (Fig. 14d, 17). They also extend west of the Yangtze Craton beneath Tibet below 100 km

depth (Fig. 14d).

(2) In contrast with the West Yangtze Block, the eastern Yangtze craton and South China Foldbelt have a much thinner seismic lithosphere (<70 km), a thin crust (~30 km, seen clearly on profile D-D' in Fig. 17), and higher mid- to lower-crustal shear wave speeds. Indeed, the seismic structure of the eastern Yangtze craton is quite similar to the South China Foldbelt. There are two somewhat subtle differences, however. First, as seen in profile D-D' in Figure 17, the seismic mantle lithosphere beneath the eastern Yangtze craton is thicker, averaging at least 80 km thickness, whereas beneath the South China Foldbelt the seismic lithosphere extends only to about 60-70 km, on average. Second, the asthenosphere beneath the South China Foldbelt is much slower than beneath the eastern Yangtze Craton, as can be seen clearly in Figure 17 by contrasting profiles A-A' and C-C' and by inspecting profile D-D'.

Only a small segment of Tibet is included in the study region, mostly encompassed by the Chuandian tectonic belt along the western margin of the Yangtze craton. Not surprisingly, the crust is determined to be very slow and thick in this region (>60 km in parts). Overall the structure is similar to that observed by *Yang et al. (2011)* in a study dedicated to Tibet.

**5.2 Contrast between the western Yangtze craton with the eastern Yangtze craton and the South China Foldbelt**

As discussed in section 5.1, there are profound structural differences between the

western part of the Yangtze Craton and both the eastern Yangtze Craton and the South China Foldbelt. This led us to refer to the "West Yangtze Block", a region with thick crust and mantle lithosphere that is presumably colder and stronger than the other parts of South China. These other parts notably include the eastern Yantze Craton, which is structurally much more similar to the South China Foldbelt than to the western Yangtze Craton. Differences do exist between the South China Foldbelt and the eastern Yangtze Craton, but they are much more subtle. Lithospheric and asthenospheric shear wave speeds in the South China Foldbelt are somewhat lower than in the eastern Yangtze craton, which reflects a slightly weaker and perhaps warmer uppermost mantle beneath the South China Foldbelt.

The structural differences within South China reflect the geological evolution of the South China Block. Geochronologic studies reveal that the Yangtze Craton possesses prominent crustal components that date at least to the Neoproterozoic (e.g., *Liu et al., 2008*) and that probably formed in the Archean (*Gao et al., 1999; Qiu et al., 2000; Zhang et al., 2006a; Zheng et al., 2006*). Archean rocks are also observed in the Kongling terrane of the Yangtze Gorges region (e.g., *Zhang et al., 2006b*). Since the Proterozoic, however, the Yangtze Craton has experienced two significant inter-continental collisions. First, the Cathaysia Block moved northward and merged with the Yangtze craton during in late Precambrian at about 1.0Ga to 0.9Ga (e.g., *Shui, 1988; Chen et al., 1991*). The two blocks merged at about 0.9Ga and have suffered little relative movement since. Second, the South China Block collided with the North China Block in the Permian to form the Qinling-Dabie suture zone (e.g., *Enkin et al.,*

24

*1992*). The eastern part of the Qinling-Dabie belt is truncated by the Tancheng-Lujiang Fault (TLF), identified by the north-south striking double line in the northeast part of Figure 1a. The sinistral slip of the TLF is about 600 km, with material from the South China Block on the east side of the TLF moving northward in a long term extensional process. This extension may be a mechanism for the thinning of the crust and lithosphere in the North Jiangsu Basin east of the TLF, which is shown in Figure 14d.

Neither of these collisions, however, explain the significant differences in crustal and lithospheric thickness between the western Yangtze craton and the eastern Yangtze craton. An important clue is provided by the existence of a 1300 km wide intracontinental orogen that occurred during the Mesozoic (*Li & Li, 2007*) between 250 Ma to 195 Ma, progressing from the southeast coast of the South China Foldbelt to the eastern boundary of the Sichuan Basin (GSA data Repository item 2007041; *Li & Li, 2007*). There is a nearly linear decrease of age from southeast to northwest with a gradient of about -0.7Ma/Km, suggesting that this intracontinental orogen progressed slowly, with an average relative speed of about 1.8mm/a.

Although a number of tectonic models have been designed to explain the evolution of this orogen (e.g., *Hsu et al., 1990; Li, 1998*) as well as the resulting postorogenic magmatism (e.g., *Jahn et al, 1990; Zhou and Li, 2000; Gilder et al., 1996*), all suffer challenges to their acceptance (e.g., *Chen, 1991; Li et al., 2003; Wang et al., 2005; Gilder et al., 1991*). We believe that the flat slab subduction model proposed by *Li & Li (2007)* may illuminate the structural variations seen in our 3D

model. In their model, Li & Li propose that a flat slab subducted northwestward beneath South China and terminated at the boundary of the Sichuan Basin, creating a series of fold belts. During this process, heat generated by friction or small-scale convection in the uppermost mantle may have been responsible for lithospheric erosion and perhaps crustal thinning. This would be a plausible explanation for the eastward and southeastward thinning of the crust and lithosphere revealed by the 3D model. Thus, in this interpretation, the West Yangtze Block is the residual of the Yangtze Craton that has not been eroded by Mesozoic flat slab subduction. *Li & Li (2007)* also hypothesize that upon termination of subduction, excess gravitational potential energy may have broken the middle part of the flat slab, causing roll-back and generating postorogenic magmatism. This additional reheating may explain why we observe a more prominent asthenosphere beneath the South China Foldbelt than beneath the eastern Yangtze Craton, even though both regions suffered effects from flat slab subduction.

Flat slab subduction, however, probably does not explain the circular low velocity zone that appears in the middle to lower crust (~25km) adjacent to the Sichuan Basin in the western Yangtze Craton. Because the Sichuan Basin is a strong and located at the eastern boundary of the active Tibetan Plateau, we speculate that these low crustal shear wave speeds result from the eastward movement of the Sichuan Basin relative to the the Yangtze Craton, which can be observed by GPS measurements (*Wang et al., 2001*). Under this circumstance, the crust near the eastern boundary of the Sichuan Basin will experience compressive forces and may undergo

deformation that has warmed the rocks of the lower and the middle crust and caused the NS trending low velocity belt.


**6. Conclusions**

The amalgamation of broad-band provincial seismic networks in China, which is referred to CEArray, presents a remarkable data resource. We apply quality control procedures to two years of continuous waveform data from CEArray to develop Rayleigh wave phase and group velocity maps from 6 to 40 sec period and phase velocity maps up to 70 sec period. Ambient noise and earthquake tomography are applied based on eikonal tomography to generate these maps. A Monte-Carlo inversion method is used to estimate a 3-D model of the crust and uppermost mantle to a depth of 150 km beneath all of South China.

The principal observation is a clear image of the "West Yangtze Block", a region of the western Yangtze Craton encompassing the Sichuan Basin with thick seismic lithosphere (> 150 km), a crust mostly thicker than 40 km, but a relatively slow middle and lower crust outside of the Sichuan Basin. The presumably cold and stable lithosphere of the West Yangtze Block contrasts with the eastern Yangtze Craton and South China Foldbelt that have a much thinner seismic lithosphere (<80 km), a thin crust (~30 km) and higher mid- to lower-crustal shear wave speeds. The eastern Yangtze Craton and South China Foldbelt are structurally quite similar, but the South China Foldbelt has a thinner mantle lithosphere (60-70 km compared with ~80 km) and better developed deeper asthenospheric layer.

This contrast in lithospheric structure between the West Yangtze Block with other parts of South China is consistent with and illuminated by that the flat slab model of Mesozoic subduction proposed by *Li & Li (2007)*. Flat slab subduction progressing northwestward beneath South China terminating at the boundary of the Sichuan Basin may have eroded the once much thicker mantle lithosphere of the eastern Yangtze Craton. The observed differences in the characteristics of the mantle lithosphere beneath the eastern Yangtze Craton and the South China Foldbelt may be traced to the formation of both regions prior to the Mesozoic or may reflect the post-orogenic magmatism that occurred beneath the South China Foldbelt that Li & Li hypothesize was caused by the breaking of the flat-slab and subsequent slab roll-back.

It is planned that future work will involve assimilation of receiver functions in the inversion to sharpen the image of the contrast between the crust and mantle and extension of data processing to include horizontal components in order to observe Love waves so that radial anisotropy in the crust and uppermost mantle can be inferred. Measurements of azimuthal anisotropy emerge naturally from the application of eikonal tomography, and inversion of these measurements to produce a model of azimuthal anisotropy in the crust and uppermost mantle also defines a natural follow-up to the research presented here.

**References**

Barmin, M. P., M. H. Ritzwoller, and A. L. Levshin (2001), A fast and reliable method for surface wave tomography, *Pure Appl. Geophs*., 158:1351-1375.

Bensen, G. D., M. H. Ritzwoller, M. P. Barmin, A. L. Levshin, F. Lin, M. P. Moschetti, N. M. Shapiro, and Y. Yang (2007), Processing seismic ambient noise data to obtain reliable broad-band surface wave dispersion measurements, *Geophys. J. Int.*, 169: 1239-1260.

Chen, J.F., K.A. Foland, F.M. Xing, X. Xu, and T.X Zhou, (1991), Magmatism along the southeast margin of the Yangtze block: Precambrian collision of the Yangtze and Cathysia blocks of China, *Geology*, 19:815-818.

Christensen, N.I. and W.D. Mooney (1995), Seismic velocity structure and

composition of the continental crust: a global view, *J. Geophys. Res.*, 100, 9761-9788.

Dziewonski, A.M. & Anderson, D.L. (1981), Preliminary reference Earth model, *Phys. Earth planet. Int.,* 25(4), 297–356.

Ekstr¨om, G., and A. M. Dziewonski, (1998), The unique anisotropy of the Pacific upper mantle, *Nature*, 394, 168–172.

Enkin, R.J., Z.Y. Yang, Y. Chen, and V. Courtillot, (1992), Paleomagnetic constraints on the geodynamic history of the majot blocks of China from the Permian to the present, *J. Geophys. Res.*, 97: 13,953-13,989.

Gao, S., Ling, W. L., Qiu, Y., Zhou, L., Hartmann, G., and Simon, K., (1999), Contrasting geochemical and Sm-Nd isotopic compositions of Archean metasediments from the Kongling high-grade terrain of the Yangtze craton: Evidence for cratonic evolution and redistribution of REE during crustal anatexis. *Geochimica et Cosmochimica Acta*, v. 63, p. 2071–2088.

Gilder, S.A., G.R. Keller, M. Luo, and P.C. Goodell, (1991), Timing and spatial distribution of rifting in China. *Tectonophysics*, 197:225-243.

Gilder, S.A., J. Gill, R.S. Coe, X.X. Zhao, Z.W. Liu, G.X. Wang, K.R. Yuan, W.L. Liu, G.D. Kuang, and H.R. Wu, (1996), Isotropic and paleomagnetic constraints on the Mesozoic tectonic evolution of south China. *J. Geophys. Res.*, 101:16,137-16,154.

Hsu, K.J., J. Li, H.Chen, Q. Wang, S. Sun, and A.M.C Sengör (1990), Tectonics of South China: Key to understanding West Pacific geology, *Tectonophysics*, 183, 9-39, doi: 10.1016/0040-1951(90)90186-C.

Huang, Z. X., W. Su, Y. J. Peng, Y. J. Zheng, and H. Y. Li (2003), Rayleigh wave tomography of China and adjacent regions, *J. Geophys. Res.*, 108, doi:10.1029/2001JB001696.

Jahn, B.M., X.H. Zhou, and J.L. Li (1990), Formation and tectonic evolution of southeastern China and Taiwan: Isotropic and geochemical constraints. *Tectonophysics*, 183:145-160.

Kanamori, H. and D. Anderson (1977), Importance of physical dispersion in surface wave and free oscillation problems : Review, *Revs. Geophys. Space Phys.*, 15(1).

Lebedev, S., and G. Nolet (2003), Upper mantle beneath Southeast Asia from S velocity tomography, *J. Geophys. Res.*, 108, doi:10.1029/2000JB000073.

Levshin, A.L., M.H. Ritzwoller, and J.S. Resovsky (1999), Source effects on surface wave group travel times and group velocity maps, *Phys. Earth Planet. Int.*, 115, 293 - 312.

Li, C. and R.D. van der Hilst (2010), Structure of the upper mantle and transition zone beneath Southeast Asia from traveltime tomography, J. Geophys. Res., 115, B07308, doi:1029/2009JB006882.

Li, S.L. and W. D. Mooney (1998), Crustal structure of China from deep seismic sounding profiles, *Tectonophysics*, 288, 105-113.

Li, X.H., Z. Chen, D.Y. Liu and W.X. Li. (2003), Jurassic gabbro-granite syenite suites from southern Jiangxi province, SE China: Age, origin, and tectonics significance. *International Geology Review*, 45:898-921.

Li, Z.X., (1998), Tectonic history of the major East Asian lithospheric blocks since the

mid-Proterozoic-A synthesis. *American Geophysical Union Geodynamics Series*, 27:221-243.

Li, Z.X., and X.H. Li, (2007), Formation of the 1300-km-wide intracontinental orogen and postorogenic magmatic province in Mesozoic South China: A falt-slab subduction model. *Geology*, 35(2): 179-182.

Lin, F.C., M.P. Moschetti, and M.H. Ritzwoller (2008), Surface wave tomography of the western United States from ambient seismic noise: Rayleigh and Love wave phase velocity maps, *Geophys. J. Int.*, doi:10.1111/j1365-246X.2008.03720.x.

Lin, F.C., M.H. Ritzwoller, and R. Snieder (2009), Eikonal Tomography: Surface wave tomography by phase-front tracking across a regional broad-band seismic array, *Geophys. J. Int.*, 177(3), 1091-1110.

Lin, F.C. and M.H. Ritzwoller (2011), Helmholtz surface wave tomography for isotropic and azimuthally anisotropic structure, *Geophys. J. Int.*, 186, 1104-1120.

Liu, X.M., S. Gao, C. Diwu, and W.L. Ling, (2008), Precambrian crustal growth of Yangtze craton as revealed by detrital zircon studies, *American Jorunal of Science*, 308: 421-468.

Mosegaard, K. and A.Tarantola (1995), Monte-Carlo sampling of solutions to inverse problems, *J. Geophys. Res.,* 100(B7), 12431-12447.

Moschetti, M.P., M.H. Ritzwoller, and F.C. Lin (2010a), Seismic evidence for widespread crustal deformation caused by extension in the western USA, *Nature*, 464, 7290, 885-889.

Moschetti, M.P., M.H. Ritzwoller, F.C. Lin, and Y. Yang (2010b), Crustal shear

velocity structure of the western US inferred from amient noise and earthquake data, *J. Geophys. Res.*, 115, B10306, doi:10.1029/2010JB007448.

Niu, F. and J. Li (2011), Component azimuths of the CEArray stations estimated from P-wave particle motion, *Earthq. Sci.,* 24, 3-13.

Qiu, Y. M., Gao, S., McNaughton, N. J., Groves, D. I., and Ling, W. L., (2000), First evidence of 3.2 Ga continental crust in the Yangtze craton of south China and its implications for Archean crustal evolution and Phanerozoic tectonics: *Geology*, 28: 11–14.

Ritzwoller, M.H. and A.L. Levshin (1998), Eurasian surface wave tomography: Group velocities, *J. Geophys. Res.*, 103, 4839 - 4878.

Ritzwoller, M.H., A.L. Levshin, L.I. Ratnikova, and A.A. Egorkin (1998), Intermediate period group velocity maps across Central Asia, Western China, and parts of the Middle East, *Geophys. J. Int.*, 134, 315-328.

Ritzwoller, M.H., F.C. Lin, and W. Shen (2011), Ambient noise tomography with a large seismic array, *Compte Rendus Geoscience*, 13 pages, doi:10.1016/j.crte.2011.03.007.

Royden, L. H., B.C. Burchfiel, et al. (1997), Surface deformation and lower crustal flow in eastern Tibet. *Science*, 276:788-790.

Sabra, K. G., P. Gerstoft, P. Roux, W. A. Kuperman, and M. C. Fehler (2005), Surface wave tomography from microseisms in Southern California, *Geophys. Res. Lett.* 32, L14311.

Shapiro, N.M. and M.H. Ritzwoller (2002), Monte-Carlo inversion for a global shear

velocity model of the crust and upper mantle, *Geophys. J. Int.*, 151, 88-105.

Shapiro, N.M., M.H. Ritzwoller, P. Molnar, and V. Levin (2004), Thinning and flow of Tibetan crust constrained by seismic anisotropy, *Science*, 305, 233-236.

Shapiro, N. M., M. Campillo, L. Stehly, and M. H. Ritzwoller (2005), High-resolution surface wave tomography from ambient seismic noise. *Science* 307, 1615-1618.

Shen, W., M. H. Ritzwoller, and V. Schulte-Pelkum (2011), Joint inversion of surface wave dispersion and receiver functions: A Monte-Carlo approach, in preparation.

Shui, T. (1988), Tectonic framework of the continental basement of southeast China. *Scientia Sinica*, 31(B):885-896.

Teng, J. W., Z. J. Zhang, J. F. Hu, and G. J. Wang (2001), The 3-D structure of shear wave in South China and the southward extension of Tanlu fault, *Chinese Science Bulletin*, 46(4): 284-289

Teng, J. W., R. S. Zeng, Y. F. Yan, and H. Zhang (2003), Depth distribution of Moho and tectonic framework in eastern Asian continent and its adjacent ocean areas, *Science in China, Ser. D*, 46(5), 428-446.

Villasenor, A., M.H. Ritzwoller, A.L. Levshin, M.P. Barmin, E.R. Engdahl, W. Spakman, and J. Trampert (2001), Shear velocity structure of Central Eurasia from inversion of surface wave velocities, *Phys. Earth Planet. Int.*, 123(2-4), 169 - 184.

Wang, Q., J.W. Li, P. Jian, Z.H. Zhao, X. L. Xiong, Z.W. Bao, J.F. Xü, C.F. Li, and J.L. Ma (2005), Alkaline syenites in eastern Cathaysia (South China): Link to Permian-Triassic transtension. *Earth. Planet. Sci. Lett.*, 230: 339-354.

Wang Q., Zhang, P.Z., Freymueller, J.T., Bilham, R., et al., (2001). Present-day

deformation in China constrained by Global Positioning System Measurements. *Science,* 294:574-577.

Yang, Y. and M.H. Ritzwoller (2008a), Teleseismic surface wave tomography in the western US using the Transportable Array component of USArray, *Geophys. Res. Letts.*, 5, L04308, doi:10.1029/2007GL032278.

Yang, Y. and M.H. Ritzwoller (2008b), The characteristics of ambient seismic noise as a source for surface wave tomography, *Geochem., Geophys., Geosys.*, 9(2), Q02008, 18 pages, doi:10.1029/2007GC001814.

Yang, Y., M.H. Ritzwoller, F.-C. Lin, M.P. Moschetti, and N.M. Shapiro (2008), The structure of the crust and uppermost mantle beneath the western US revealed by ambient noise and earthquake tomography, *J. Geophys. Res.*, 113, B12310.

Yang, Y., Y. Zheng, J. Chen, S. Shou, S. Celyan, E. Sandvol, F. Rilmann, K. Priestley, T.M. Hearn, J.F. Ni, L.D. Brown, and M.H. Ritzwoller (2010), Rayleigh wave phase velocity maps of Tibet and the surrounding regions from ambient seismic noise tomography, *Geochem., Geophys., Geosys.*, 11(8), Q08010, doi:10.1029/2010GC003119.

Yang, Y., M.H. Ritzwoller, Y. Zheng, A.L. Levshin, and Z. Xie (2011), A synoptic view of the distribution and connectivity of the mid-crustal low velocity zone beneath Tibet, *J. Geophys. Res.*, submitted.

Zhang, P. Z., Q. D. Deng, G. M. Zhang, J. Ma, W. J. Gan, W. Min, F. Y. Mao, and Q. Wang (2003), Active tectonic blocks and strong earthquakes in the continent of China, *Science in China, Ser. D*, 46(Supp.), 13-24.

Zhang, S. B., Zheng, Y. F., Wu, Y. B., Zhao, Z. F., Gao, S., and Wu, F. Y. (2006a),
Zircon U–Pb age and Hf isotope evidence for 3.8 Ga crustal remnant and episodic
reworking of Archean crust in South China. *Earth Planet. Sci. Lett.*, 252:
56–71,doi:10.1016/j.epsl.2006.09.027.

Zhang, S. B., Zheng, Y. F., Wu, Y. B., Zhao, Z. F., Gao, S., and Wu, F. Y. (2006b),
Zircon isotope evidence for _3.5 Ga continental crust in the Yangtze craton of
China. *Precambrian Research*, 146: 16–34.

Zhang, Z. M., J. G. Liou, and R. G. Coleman (1984), An outline of the plate tectonics
of China, *Geol. Soc. Am. Bull*, 95, 295-312.

Zheng, J., W.L. Griffin, S.Y. O'Reilly, M. Zhang, N. Pearson, and Y. Pan (2006),
Widespread Archean basement beneath the Yangtze craton, *Geology*, 34(6),
417-420, doi:10.1130/G22282.1,.

Zheng, J. P., Griffin, W. L., O'Reilly, S. Y., Zhang, M., and Pearson, N., (2006),
Widespread Archean basement beneath the Yangtze Craton. *Geology*, 34:417–420.

Zheng, S., X. Sun, X. Song, Y. Yang, and M.H. Ritzwoller, Surface wave tomography
of China from ambient seismic noise, *Geochem. Geophys. Geosyst.*, 9, Q0502,
doi:10.1029/2008GC001981, 2008.

Zheng, X. F., Z. X. Yao, J. H. Liang, and J. Zheng (2010a), The role played and
opportunities provided by IGP DMC of China National Seismic Network in
Wenchuan earthquake disaster relief and researches, *Bull. Seismol. Soc. Am.*,
100(5B), 2866-2872.

Zheng, Y., Y. Yang, M.H. Ritzwoller, X. Zheng, X. Xiong, Z. Li (2010b), Crustal

structure of the northeastern Tibetan Plateau, the Ordos Block, and the Sichuan Basin from ambient noise tomography, *Earthquake Science*, 3, 465-476, doi:10.1007/s11589-010-0745-3.

Zheng, Y., W. Shen, Y. Yang, Z. Xie, M.H. Ritzwoller (2011), Ambient noise Rayleigh wave tomography for northeast China, the Korean Peninsula, and the Sea of Japan, *J. Geophys. Res.,* submitted.

Zhou, X.M., and W.X. Li (2000), Origin of late Mesozoic igneous rocks in southeastern China: Implications for lithosphere subduction and underplating of mafic magmas. *Tectonophysics*, 326:269-287, doi: 10.1016/S0040-1951(00)00120-7.

**Table 1**: Problematic stations

| Problem with vertical component | Station name | If identified as problematic by Niu and Li (2011) |
|---|---|---|
| mis-located | AHHUA, GXGXS, GZDJT, HNJGS, JSXIY ,JSYC | No |
| | HIQZN, HNJIS, YNKMI | Yes |
| Instrument response error 1 (perhaps time variable) | GDNAP ,HAJS, SNHUYT, SNHZHT, SNNSHT, SNTABT, SNQLIT, SNJYAT, ZJQIY, ZJYOK | No |
| | GZZFT, SHNAH, SNLOXT | Yes |
| Instrument response error 2 ($\pi$ error) | GDCHZ ,GDHYJ, GDLCH, GDMEZ, GDSHW, GDXIG, GDYGJ, GZXYT | No |
| | GDLTK, GDNAO, GDTIX | Yes |

**Table 2**: Final number of measurements and misfit as a function of period for ambient noise.

| Period (sec) | Numbers | | Misfit (sec) | |
|---|---|---|---|---|
| | Group | Phase | Group | Phase |
| 6.00 | 19120 | 20726 | 2.37 | 1.03 |
| 8.00 | 32066 | 34546 | 2.82 | 1.14 |
| 10.00 | 41017 | 45369 | 2.86 | 1.15 |
| 12.00 | 46666 | 50356 | 2.86 | 1.02 |
| 14.00 | 49336 | 52191 | 2.72 | 0.90 |
| 16.00 | 49951 | 52171 | 2.76 | 0.79 |
| 18.00 | 49967 | 51141 | 3.15 | 0.74 |
| 20.00 | 47767 | 48907 | 3.20 | 0.76 |
| 25.00 | 36427 | 38159 | 3.89 | 0.88 |
| 30.00 | 24911 | 27066 | 4.32 | 1.19 |
| 35.00 | 16841 | 18570 | 4.79 | 1.32 |
| 40.00 | 10981 | 12630 | 4.90 | 1.51 |

**Figure Captions:**

**Figure 1.** (a) Tectonic map of South China. Thick lines indicate the boundaries of the major tectonic units and basins, after *Zhang et al*. [1984] and *Zhang et al* [2003]. The South China Block comprises the Yangtze Craton, which encompasses the Sichuan Basin (**SB**) and the Jianghan Basin (**JB**), the South China Foldbelt, and the Youjian Block (**YB**). Other identified tectonic features are: **OB**, Ordos Basin; **NCP**, North China Platform; **NJB**, North Jiangsu Basin; **BHB**, Bayan Har Block; **CB**, Chuandian Block; **SYB**, South Yunnan Block; **YB**, Youjiang Block. The four colored diamonds identify locations referred to in Figs. 12 and 13 (CB: green; SB: black; Yangtze craton, blue; South China Foldbelt, red). (b) The 387 CEArray stations for which we have instrument response files are shown with variously colored triangles; the 354 used in this study are shown in grey or white. The large white triangle is the location of station AHJIX referred to in Fig. 6. The blue, red, and black triangles identify the problematic stations where the problem is mis-location, $\pi$ phase error, or an unknown (perhaps time variable) problem with the instrument response, respectively.

**Figure 2.** (a) Example of the misfit histogram for a station (CQSHZ) that is determined to be of good quality. The histogram presents the difference between the inter-station Rayleigh wave phase travel time at 20 sec period observed with ambient noise and the travel time at the same period predicted by the phase velocity map computed with straight ray tomography (Fig. 9c). The average and standard deviation of the misfit are listed. (b) The location of station CQSHZ is shown with a large star

and differences between the observed and predicted travel times between this and all other stations are color coded. Positive values (red colors) indicate that the observed time is longer than that predicted (velocity is slower).

**Figure 3.** Examples of problematic stations. (a) & (b) Similar to Fig. 2, but for station HNJIS which is believed to have a location error of about 1.5 km. (c) & (d) Similar to (a) & (b), but for station SNLOXT which has an unknown, perhaps time-variable, problem with the instrument response. (e) & (f) Also similar to (a) & (b), but for station GDLTK which is believed to have a $\pi$ phase error. The error scales with period.

**Figure 4.** Histograms of Rayleigh wave phase travel time misfit between the travel times measured on the ambient noise cross-correlations using data that pass quality control procedures and travel times predicted from the phase velocity maps at each period constructed via straight-ray theory (Barmin et al., 2001). The standard deviation of the distribution is listed on each panel.

**Figure 5.** Same as Fig. 4, but for group velocity.

**Figure 6**. Two-year cross-correlations filtered between periods of 5 and 50 sec are shown between seismic station AHJIX (white triangle in Fig. 1b) and other stations. Rayleigh waves appear at both negative and positive correlation lag times with a move-out of about 3 km/s. Arrivals near zero time are probably mostly teleseismic body waves, which are not studied here.

**Figure 7.** Comparison of the 20 sec Rayleigh wave phase velocity maps constructed with (a) straight-ray tomography (Barmin et al., 2001) and (b) eikonal tomography (Lin et al., 2009) using ambient noise. (c) Map of the difference between the results in (a) and (b). (d) Histogram of the differences between results in (a) and (b).

**Figure 8.** Rayleigh wave group velocity maps at periods of (a) 8, (b) 14, (c) 20 and (c) 30 sec determined from ambient noise using the straight ray method of Barmin et al. (2001). Maps truncate (revert to grey shades) where resolution is worse than 100 km. Average group velocities at these periods are 2.9488 km/s, 2.9177 km/s, 2.9514 km/s and 3.2937 km/s, respectively.

**Figure 9.** Rayleigh wave phase velocity maps constructed by Rayleigh wave eikonal tomography applied to ambient noise data at periods of (a) 8, (b) 14, and (c) 20 sec. Average phase velocities at these periods are 3.1261 km/s, 3.2747 km/s, and 3.4708 km/s, respectively. Similar maps constructed from earthquake data are shown for (d) 40 sec, (e) 50 sec and (f) 70 sec period, where phase velocities are 3.8427 km/s, 3.9081 km/s, and 3.9823 km/s, respectively. As in Fig. 8, maps truncate where resolution is worse than 100 km.

**Figure 10.** (a) Ambient noise derived phase velocity map at 32 sec period (avg = 3.7479 km/s). (b) Earthquake derived phase velocity map at 32 sec period (avd = 3.7609 km/s). (c) Difference between the maps shown in (a) and (b). (d) Histogram of the differences presented in (c).

**Figure 11.** Examples of raw uncertainties estimated for the Rayleigh wave phase

velocity maps by eikonal tomography for (a) ambient noise at 20 sec period (avg = ~10 m/s) and (b) earthquake data at 40 sec period (avg = ~18 m/s).

**Figure 12**. Dispersion curves at different locations: Chuandian Block, Sichuan Basin, Yangtze Craton, and South China Foldbelt. Locations are indicated by the green, black, blue, and red diamonds in Fig. 1a, respectively. Rayleigh and Love wave phase (red lines) and group (blue lines) velocities predicted from the best fitting Vs model are compared with the measured values (error bars) extracted from the dispersion maps at each location. Square-root of $\chi^2$ misfit is listed as "RMS misfit".

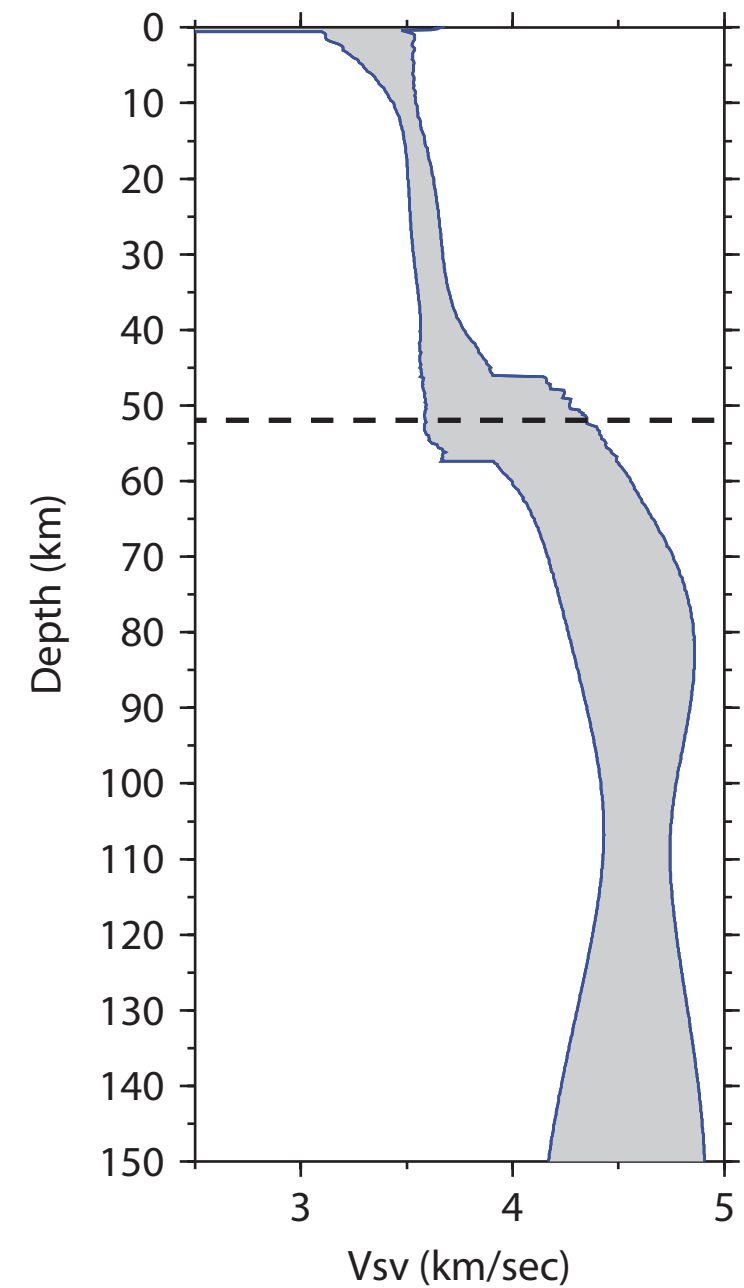**Figure 13.** Ensemble of accepted models determined from each of the corresponding pairs of dispersion curves in Fig. 12. (Top Row) Shallow Vs structure: 2σ corridor of acceptable models between the surface and 25 km depth, highlighting the shallow crust. (Bottom Row) Full Vs model: 2σ corridor of acceptable models between the surface and 80 km depth, highlighting crustal thickness (dashed line).

**Figure 14.** Horizontal slices of the estimated Vs model (middle of the ensemble of accepted models at each depth) plotted at four depths (10 km, 25 km, 70 km, and 140 km). Velocities are plotted as the percent deviation relative to the mean (shown) across the map at each depth. The straight lines in (d) identify the locations of the vertical model slices shown in Fig. 17.

Figure 15. (a) Crustal thickness estimated across the study region (in km). (b) One standard deviation uncertainties estimated for crustal thickness (in km).

**Figure 16.** Model uncertainties (1 standard deviation) plotted at the same depths as the horizontal slices shown in Fig. 14.

**Figure 17.** Vertical slices of the estimated Vs model (middle of the ensemble of acceptable models at each depth) plotted along the four profiles identified in Fig. 14d. Absolute velocities are presented in the crust and percent perturbations relative to 4.5 km/s are shown in the mantle.
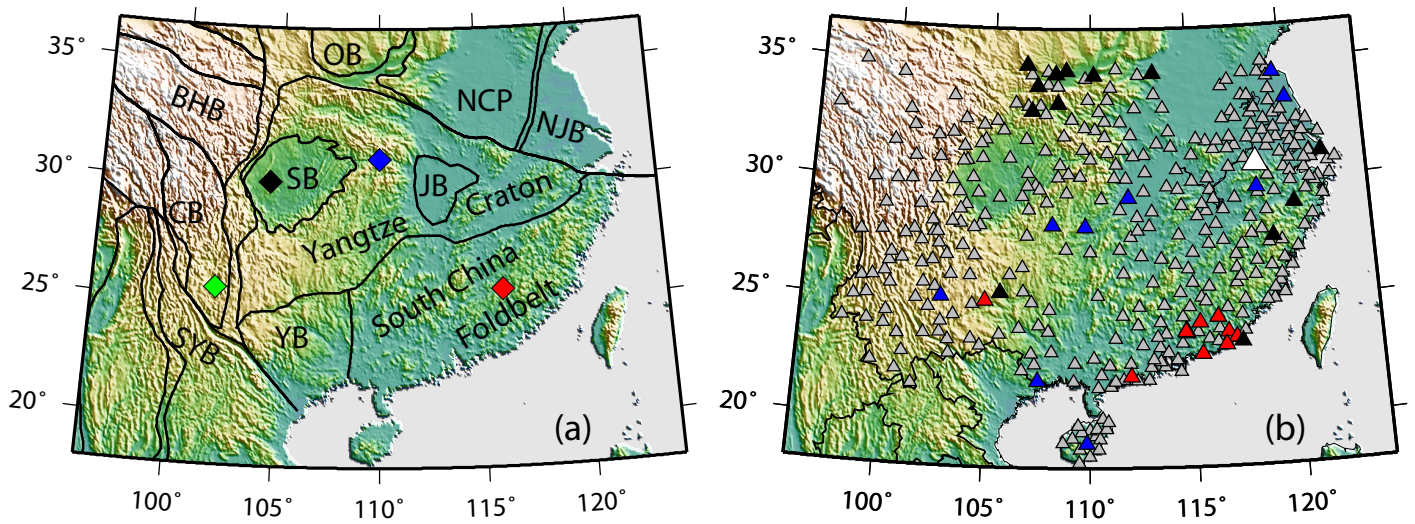
Figure 1 of 17
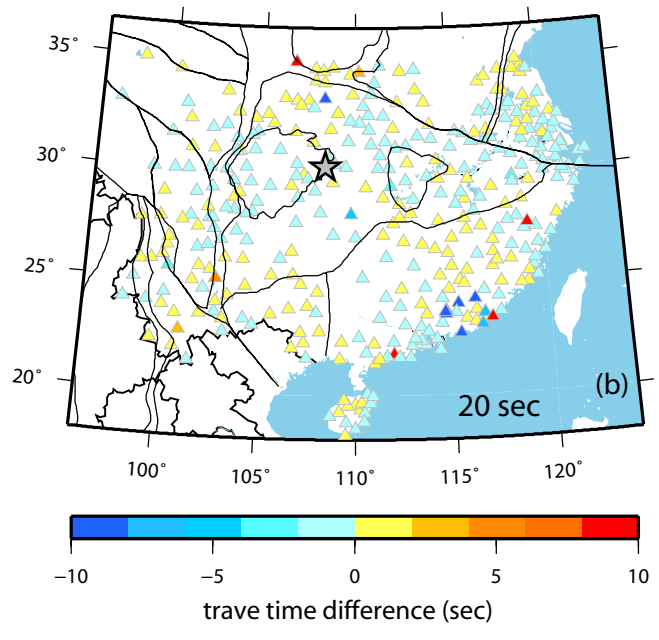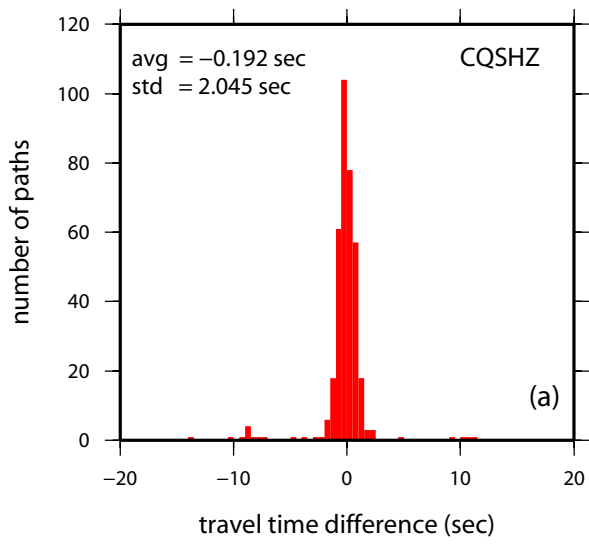
Figure 2 of 17
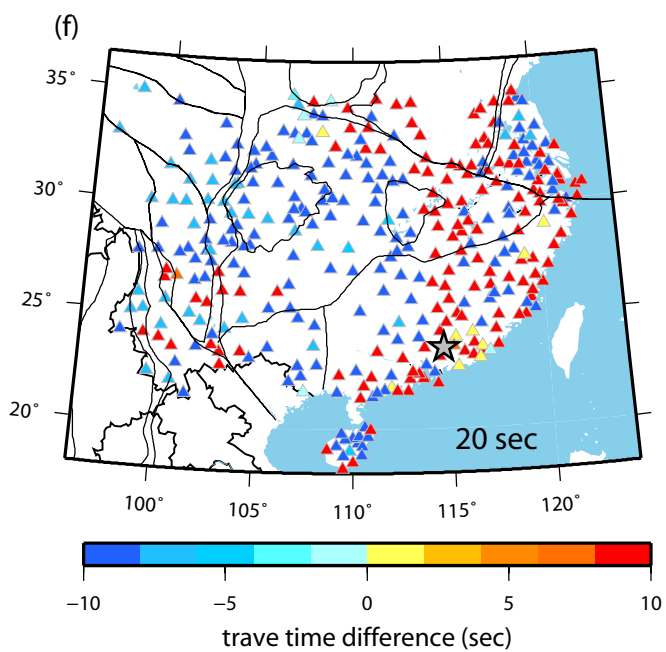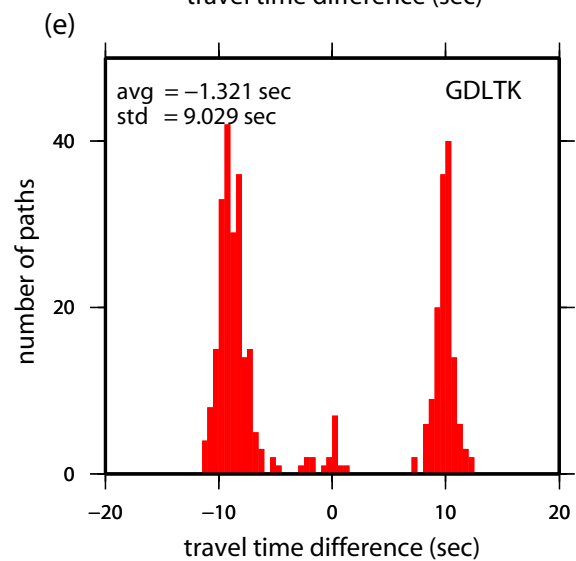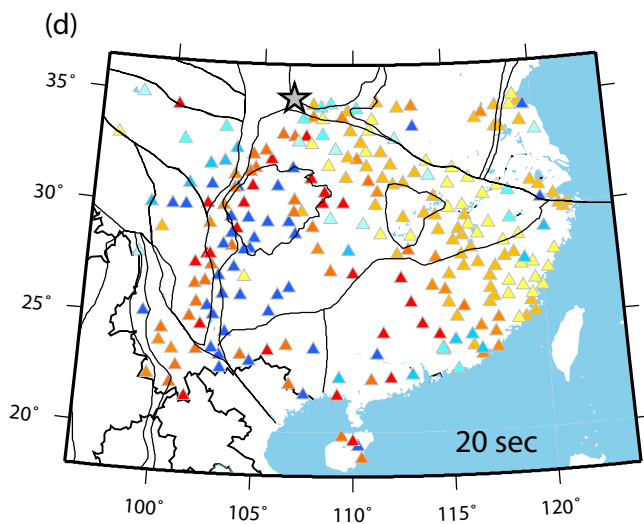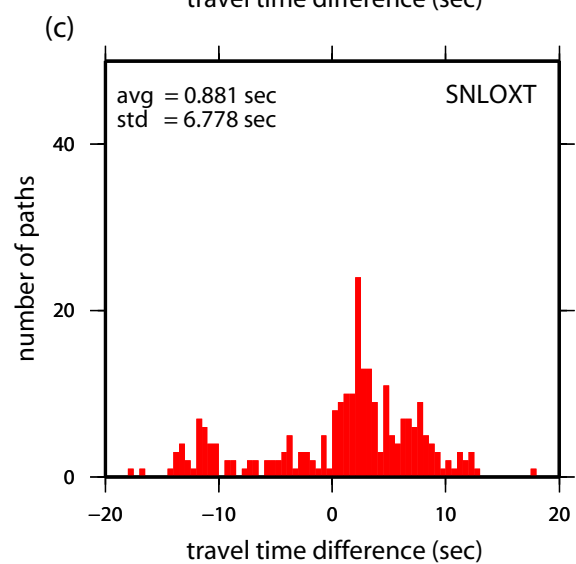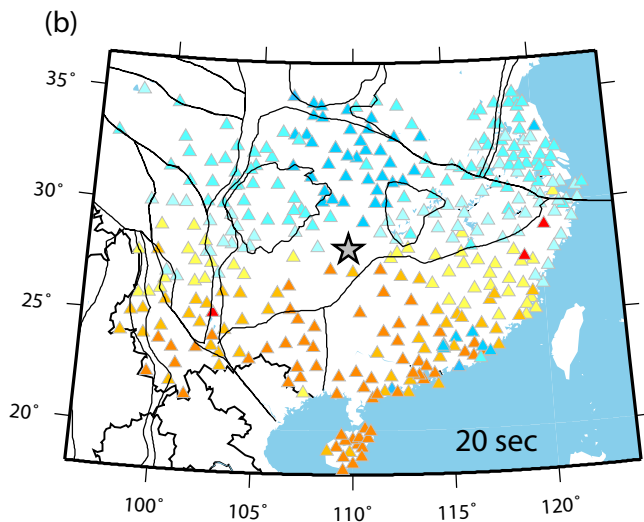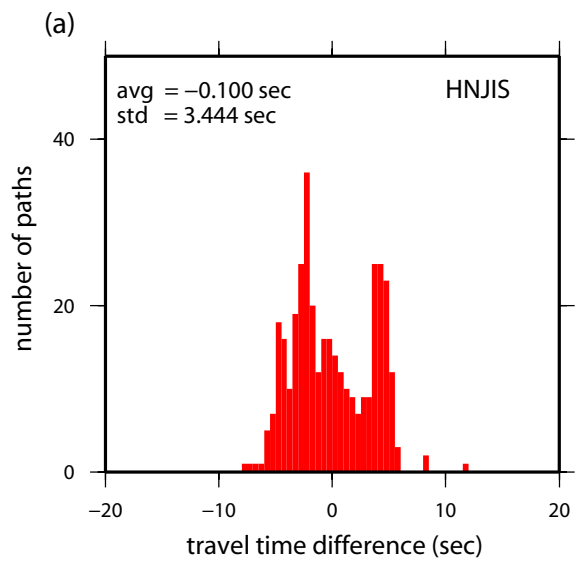
Figure 3 of 17
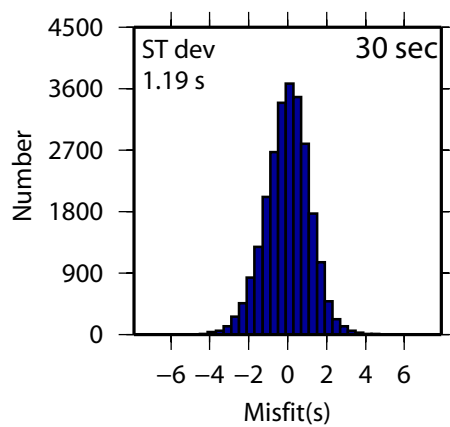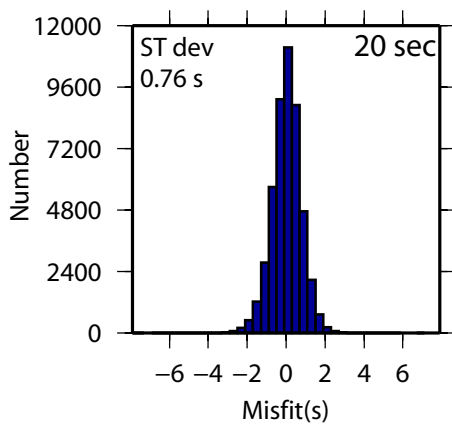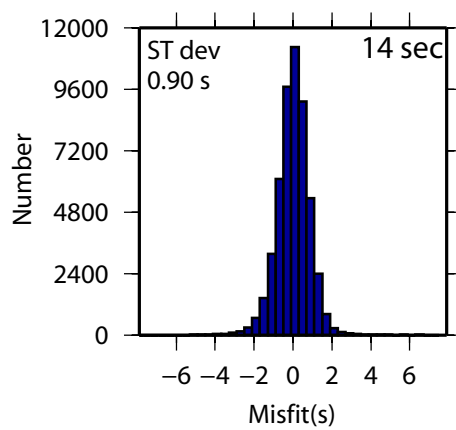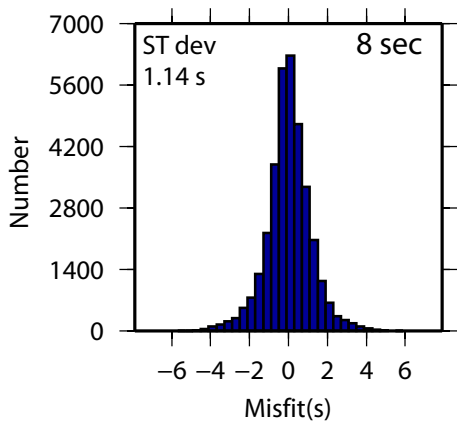
Figure 4 of 17
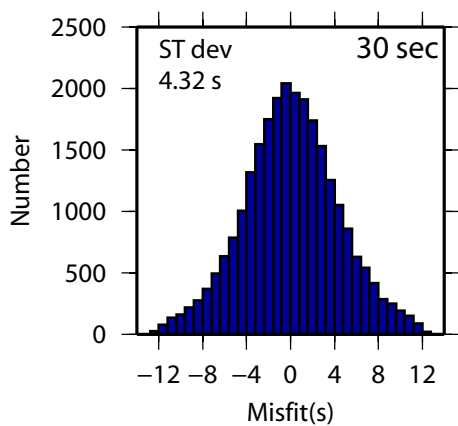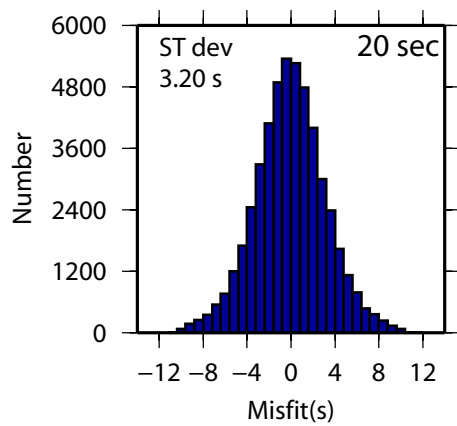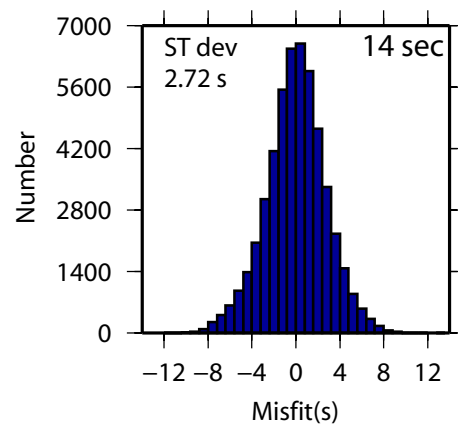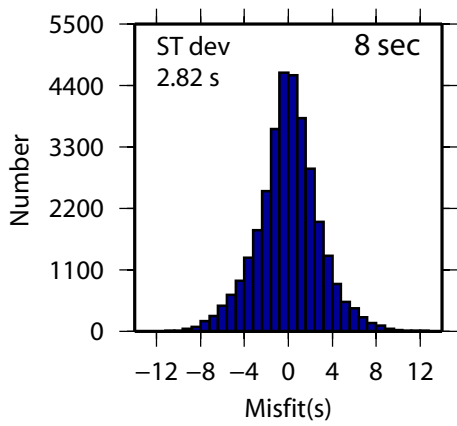
Figure 5 of 17
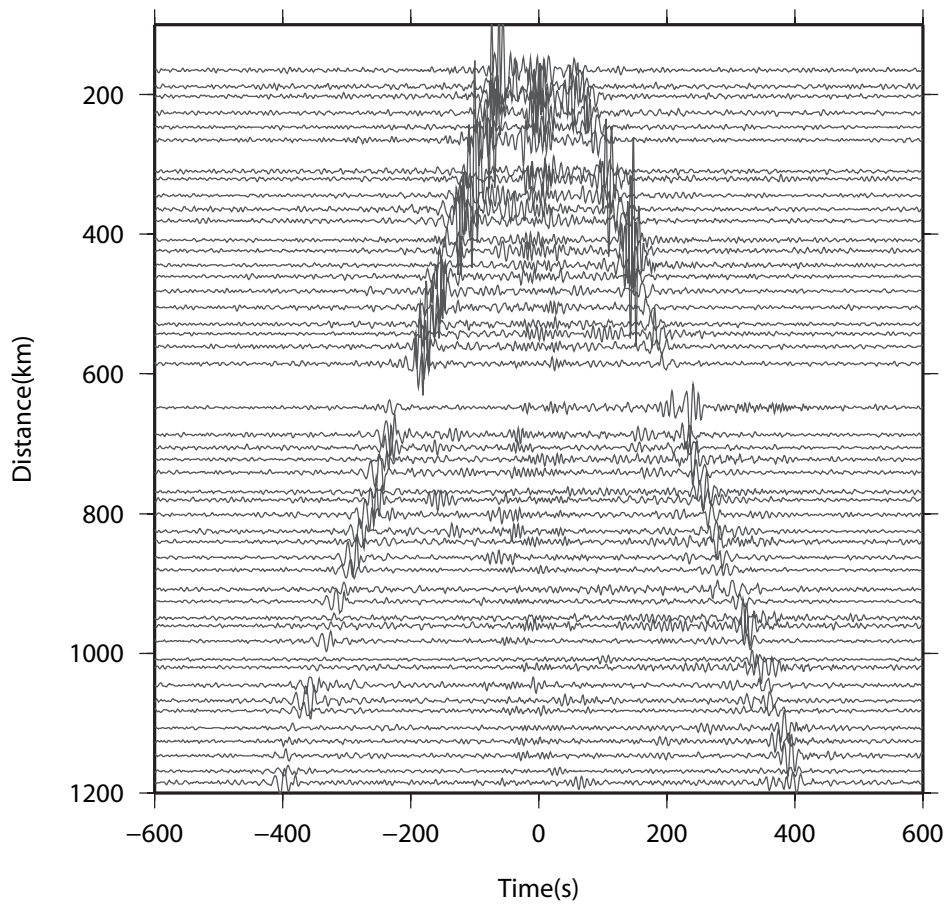
Figure 6 of 17
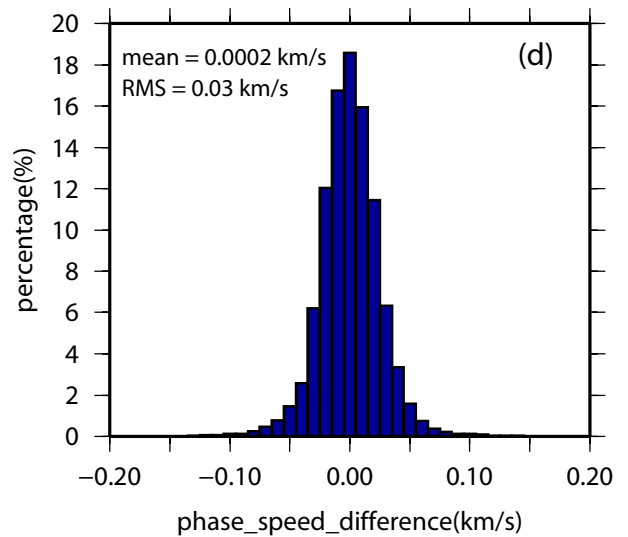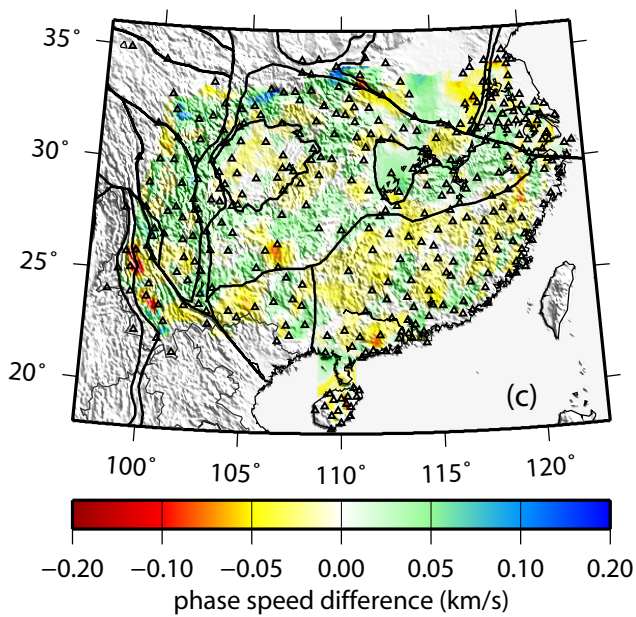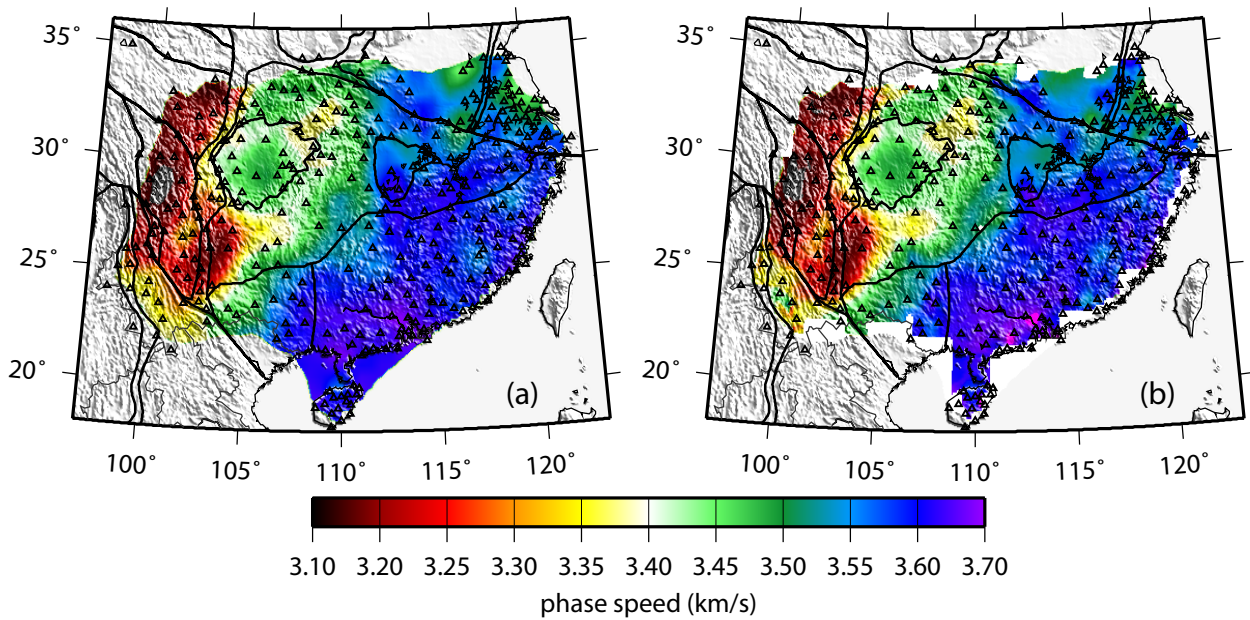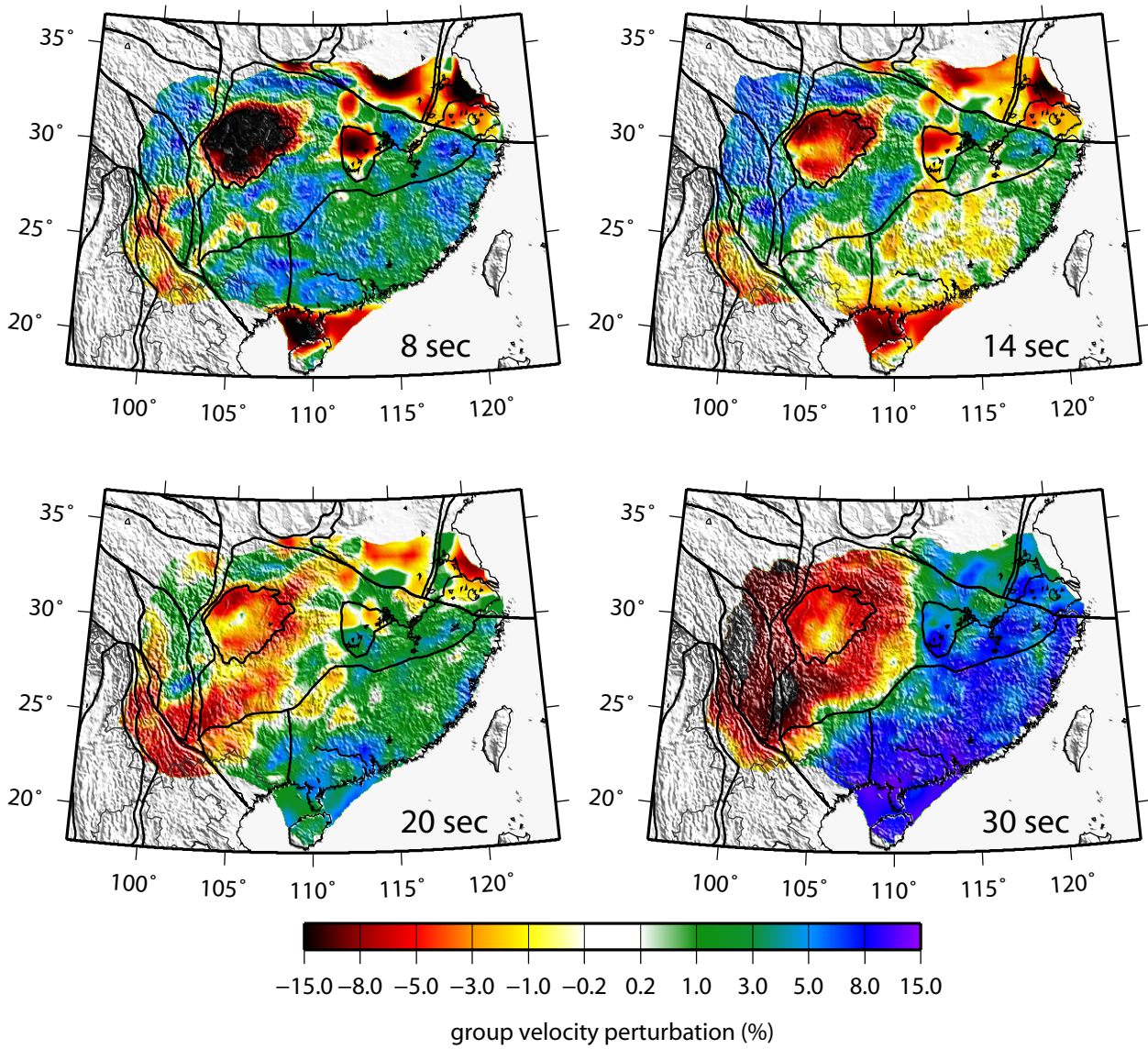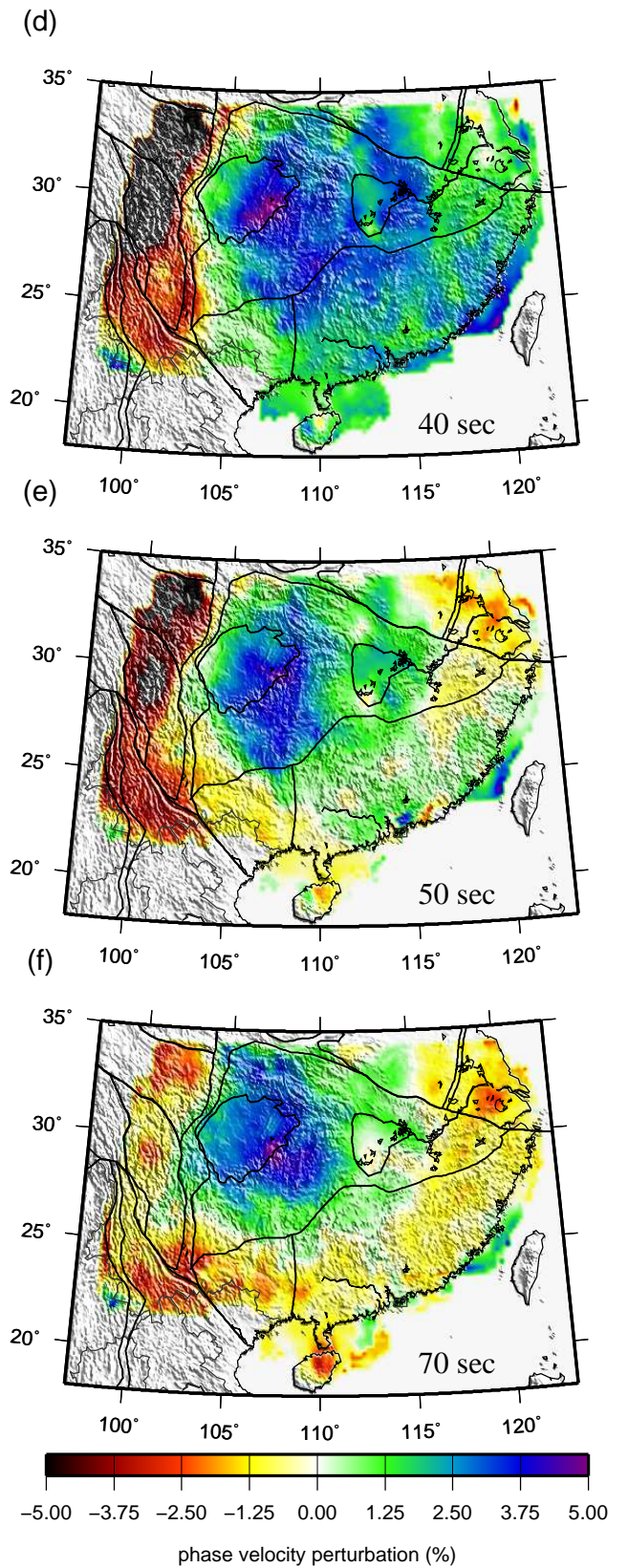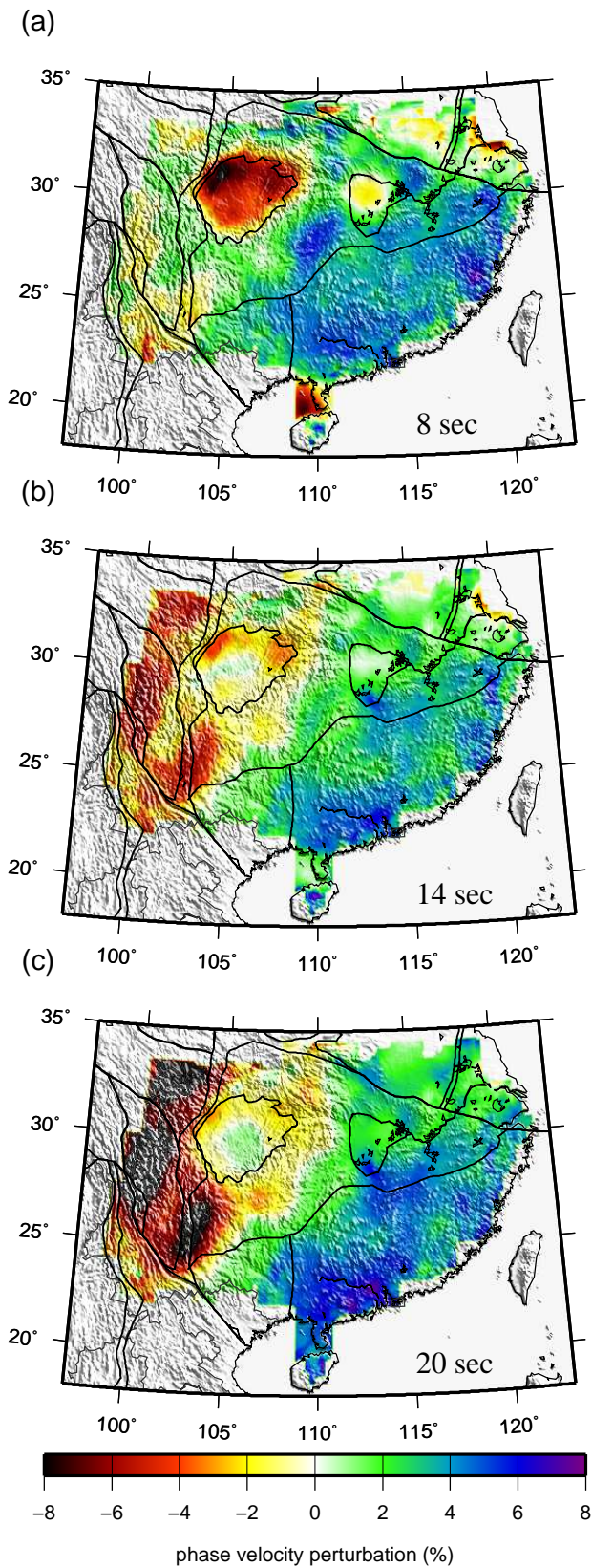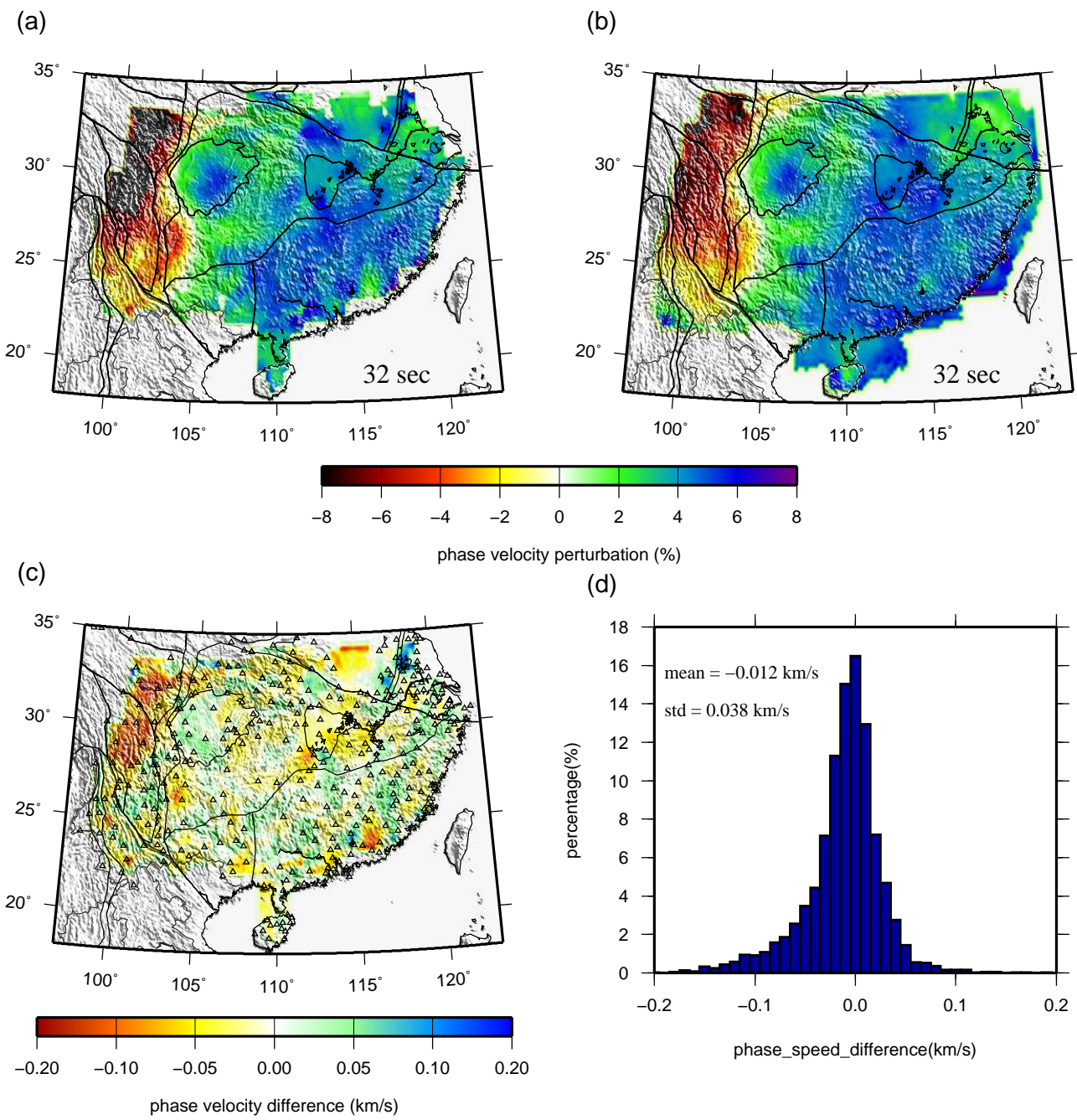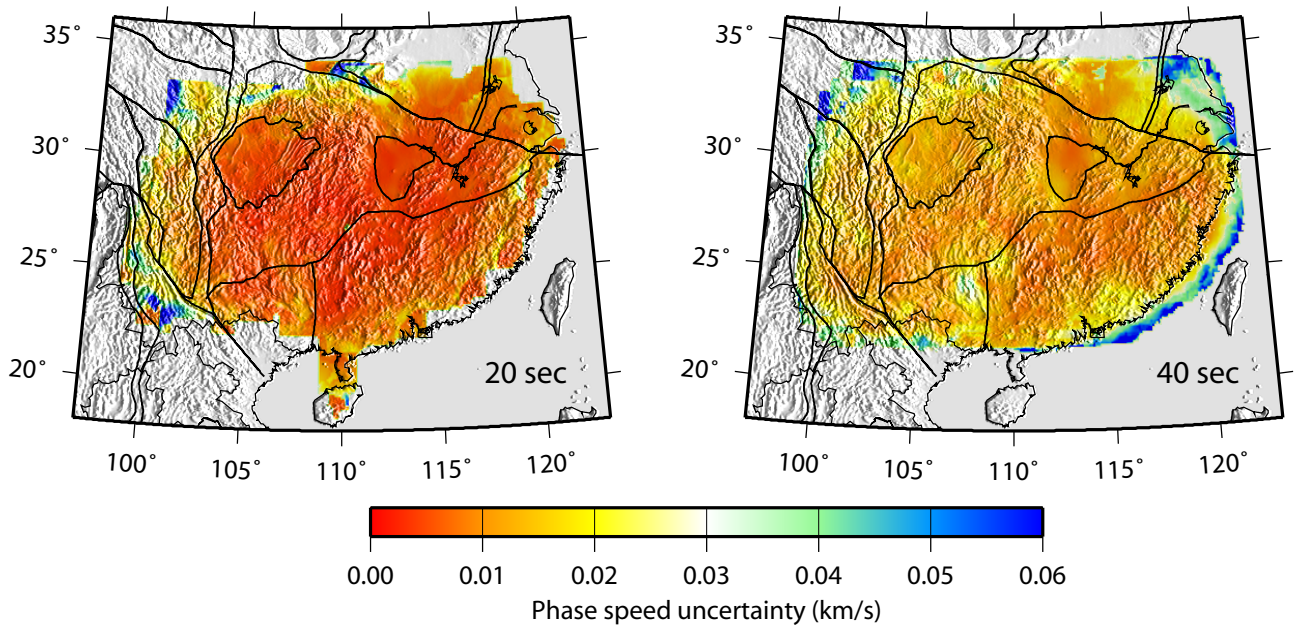
phase speed (km/s)

phase speed difference (km/s)

Figure 7 of 17

group velocity perturbation (%)

Figure 8 of 17

(a) 8 sec
(b) 14 sec
(c) 20 sec
(d) 40 sec
(e) 50 sec
(f) 70 sec

phase velocity perturbation (%)

phase velocity perturbation (%)

Figure 9 of 17

(a)

(b)

phase velocity perturbation (%)

(c)

phase velocity difference (km/s)

(d)

mean = −0.012 km/s

std = 0.038 km/s

phase_speed_difference(km/s)

Figure 10 of 17

Phase speed uncertainty (km/s)

Figure 11 of 17

(a) Chuandian Block

RMS misfit = 1.67625

(b) Sichuan Basin

RMS misfit = 1.57047

(c) W. Yangtze Craton

RMS misfit = 1.731

(d) S. China Foldbelt

RMS misfit = 0.957904

Figure 12 of 17

Figure 13 of 17
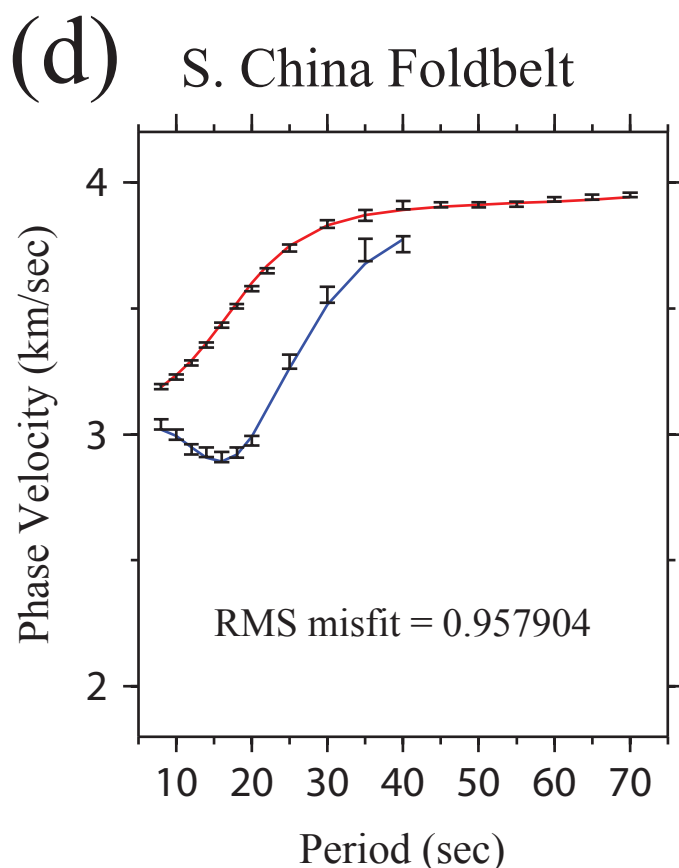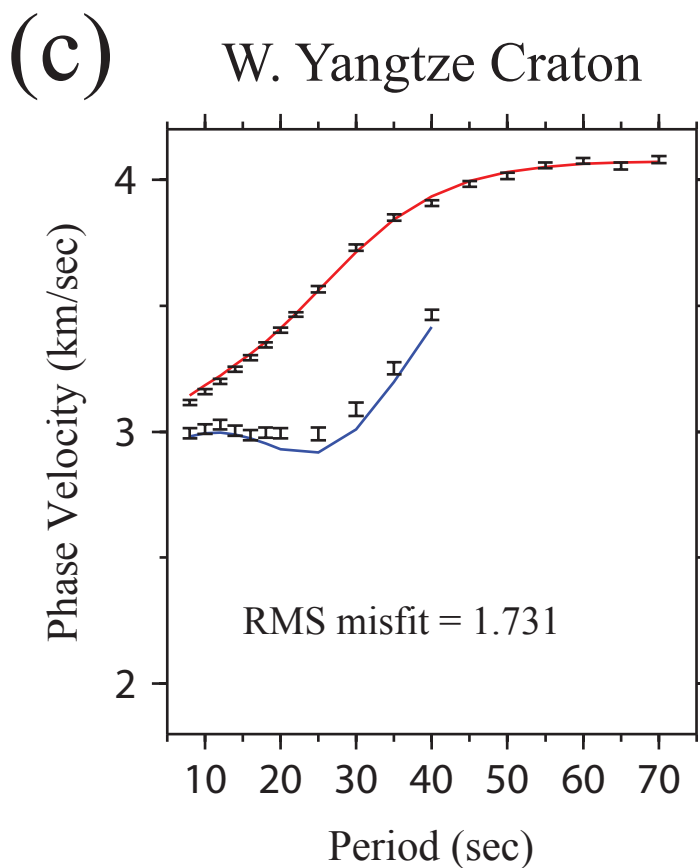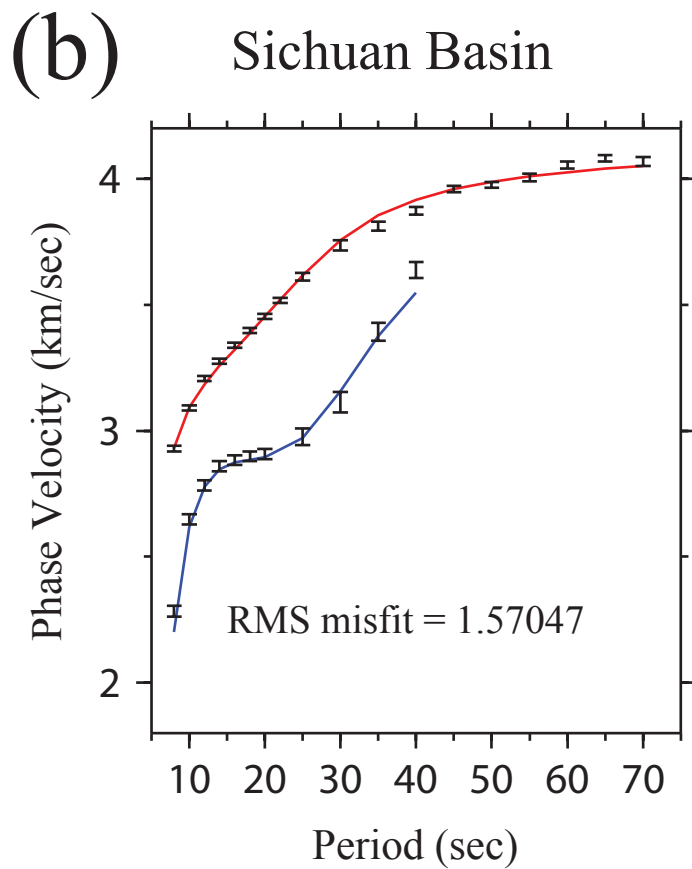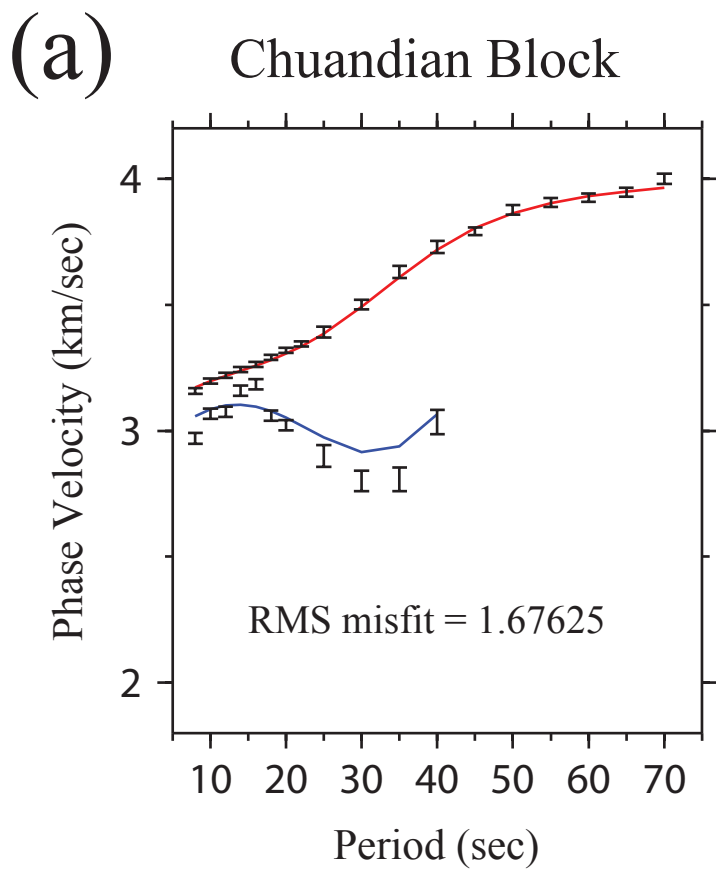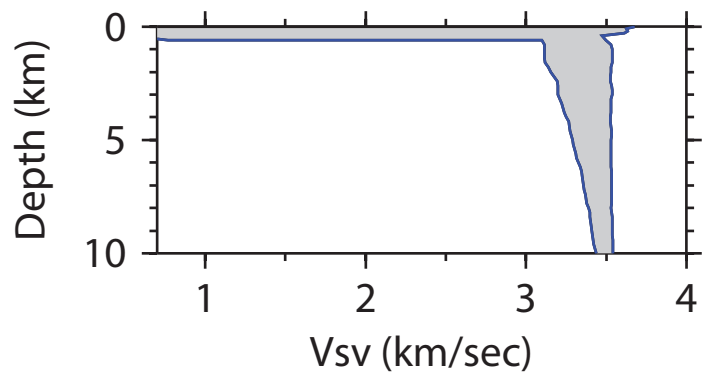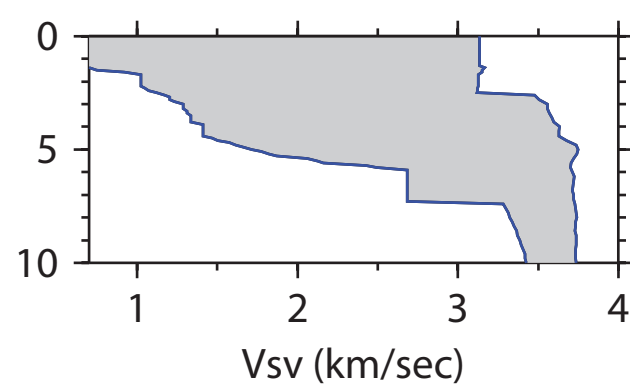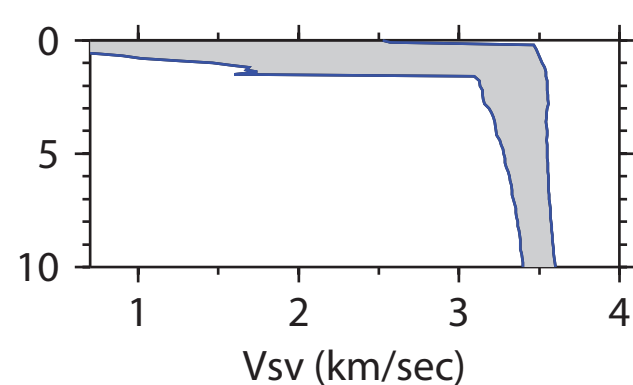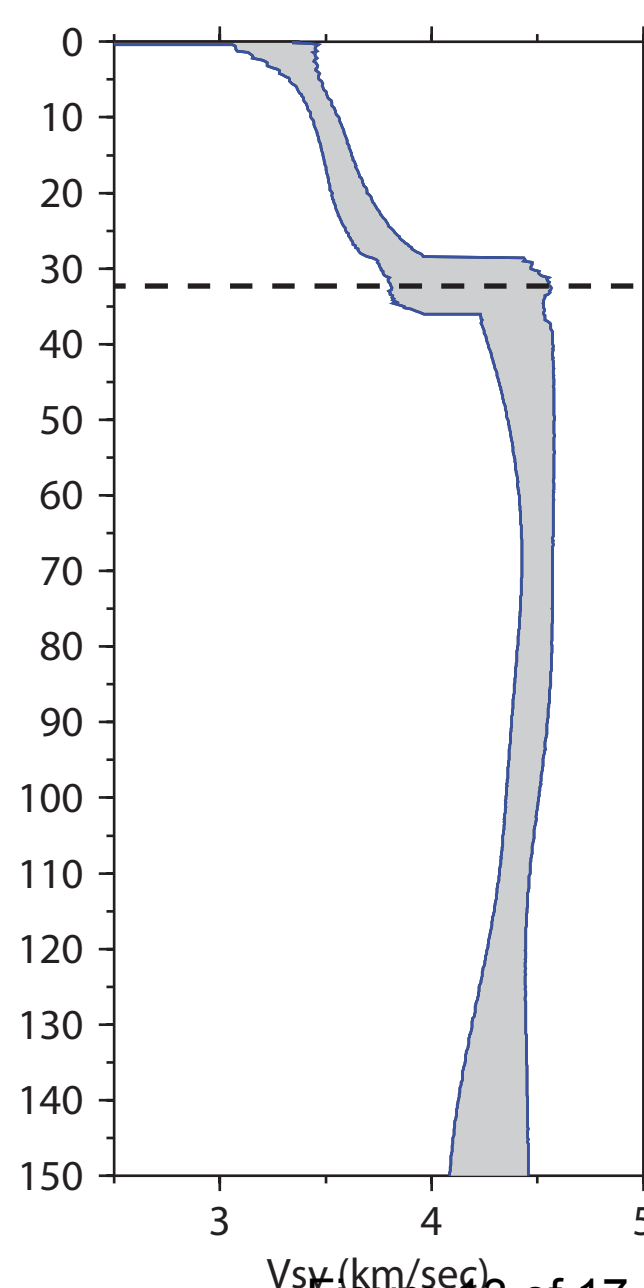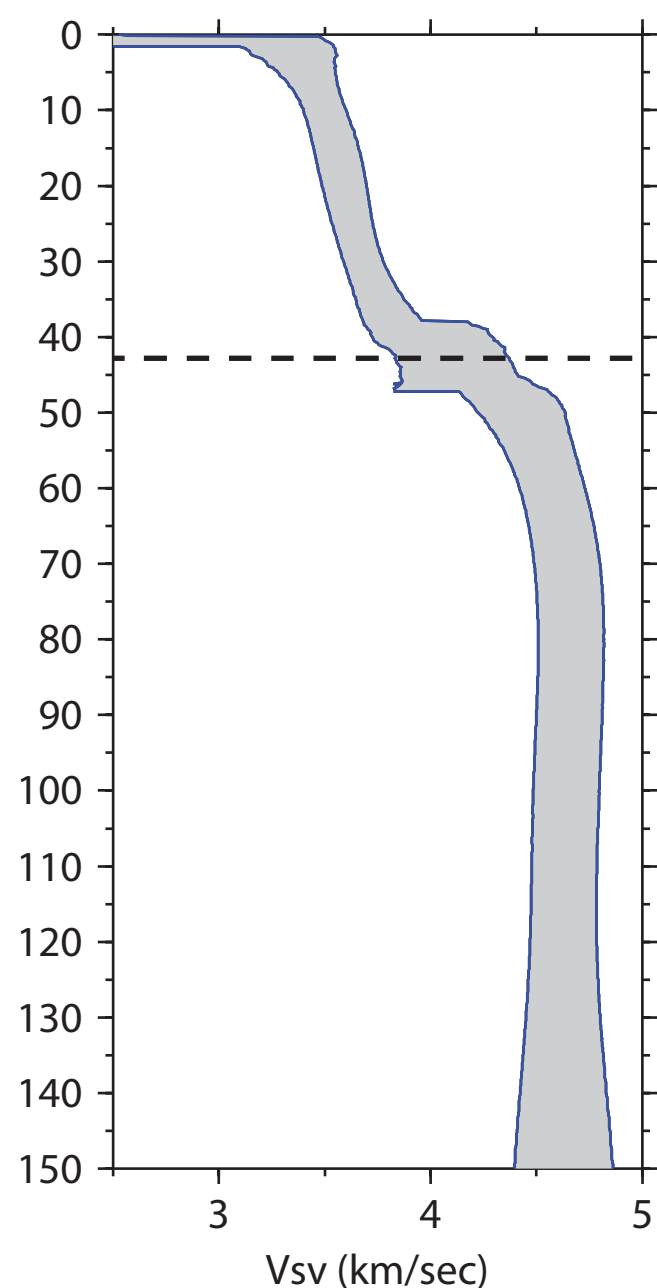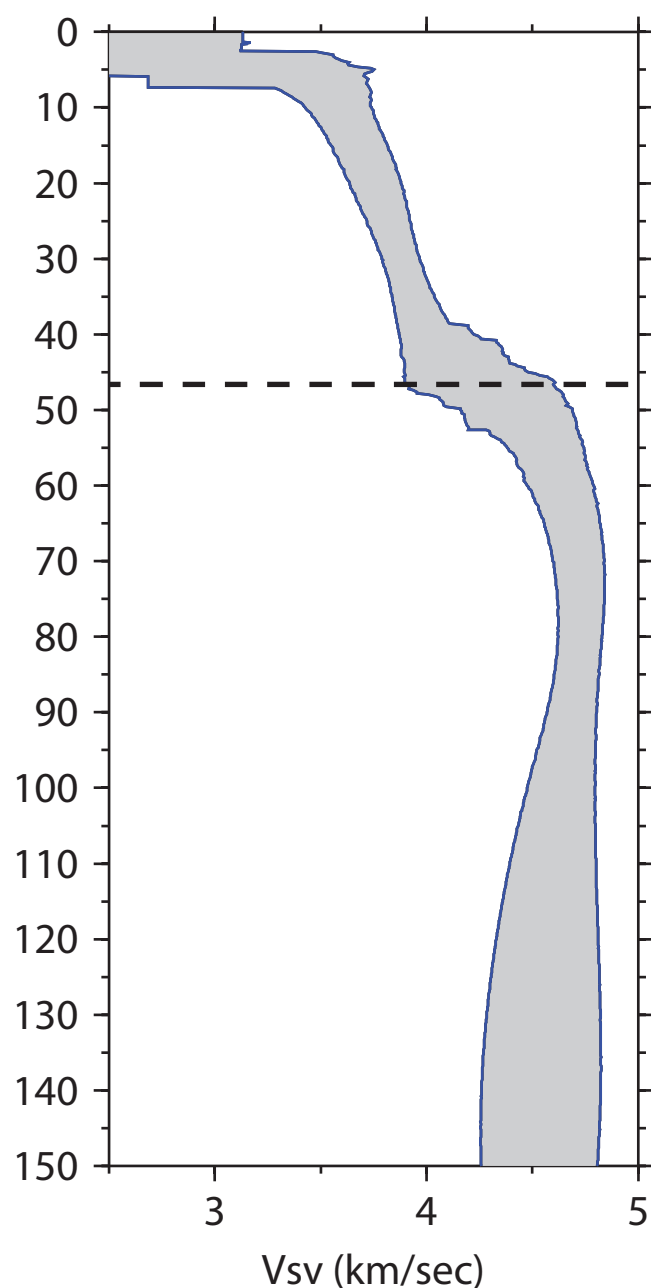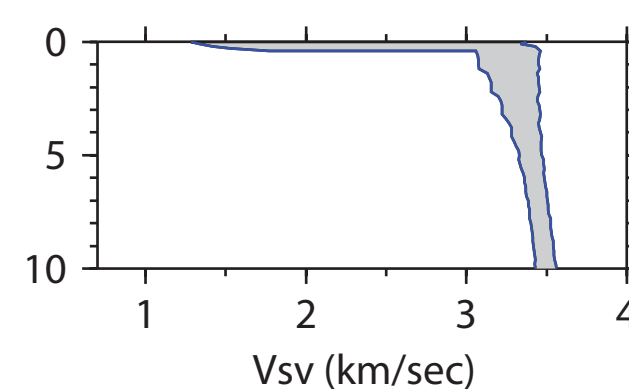
depth = 10km
3.46 km/sec
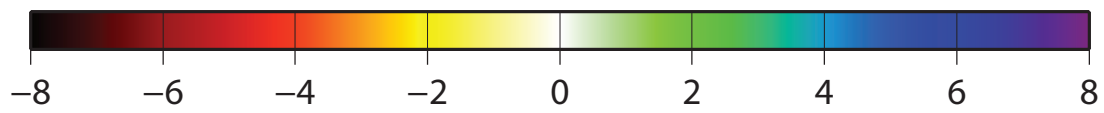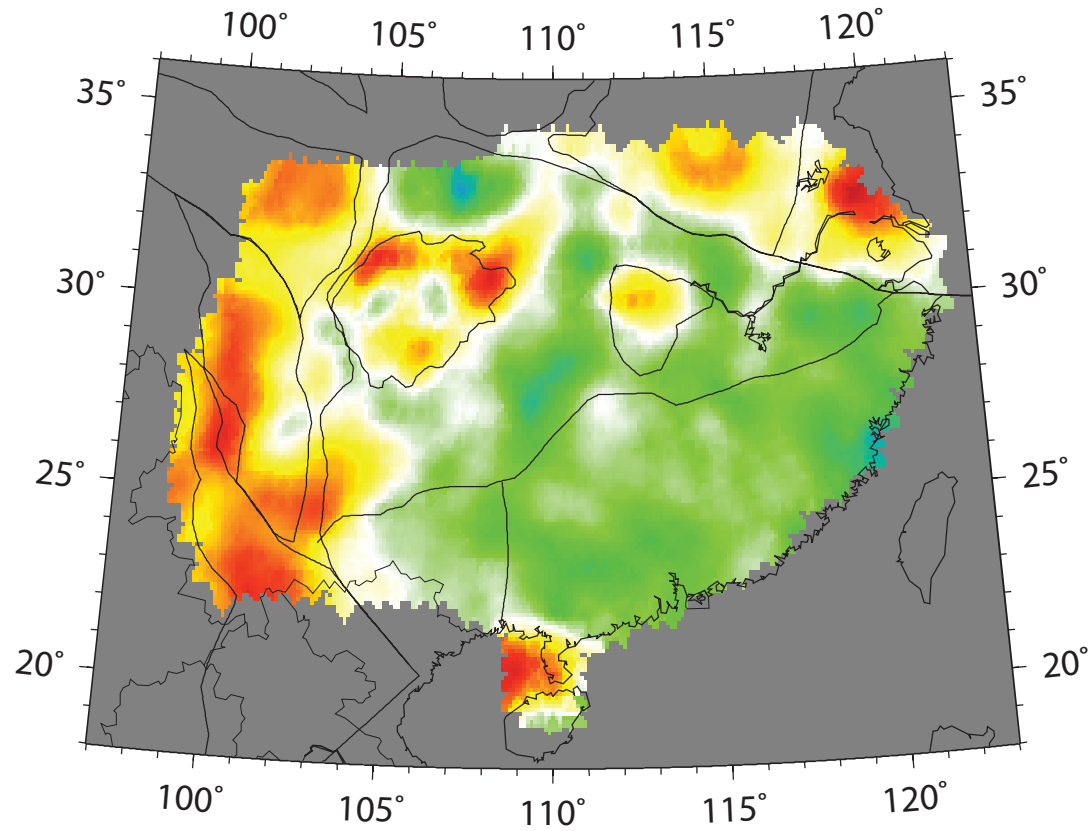
depth = 25km
3.69 km/sec
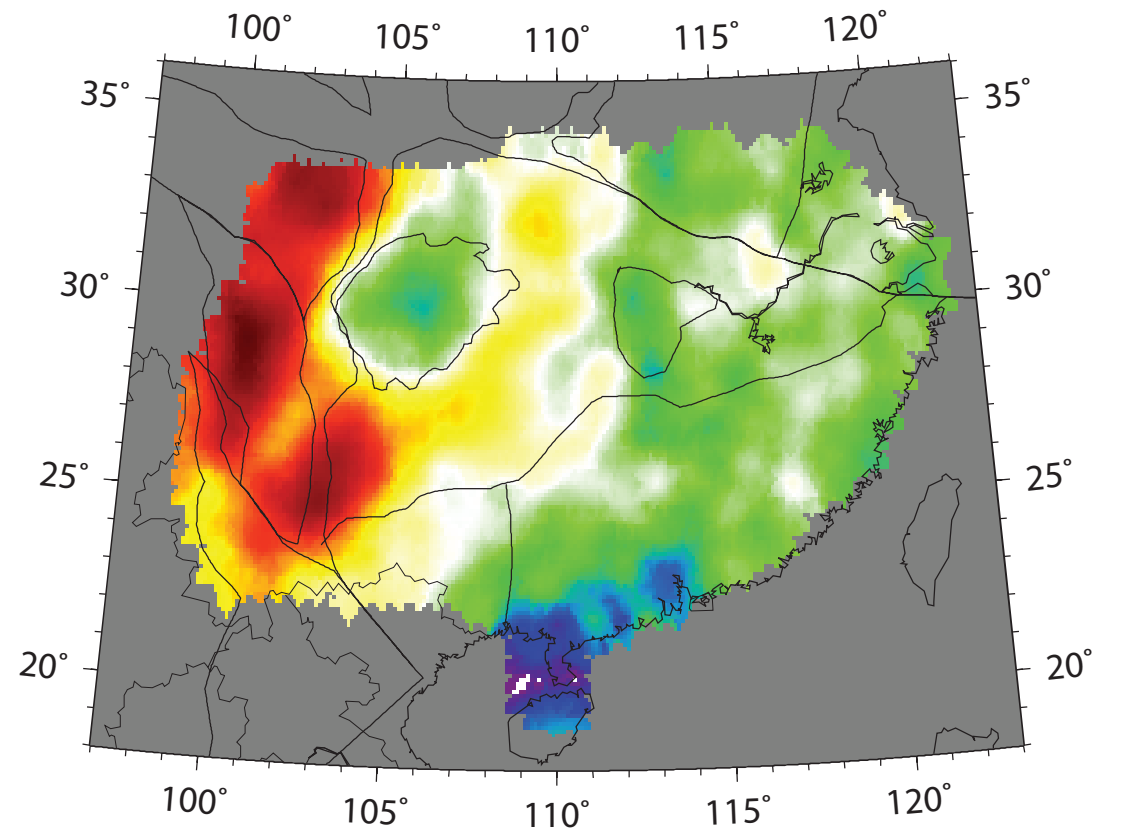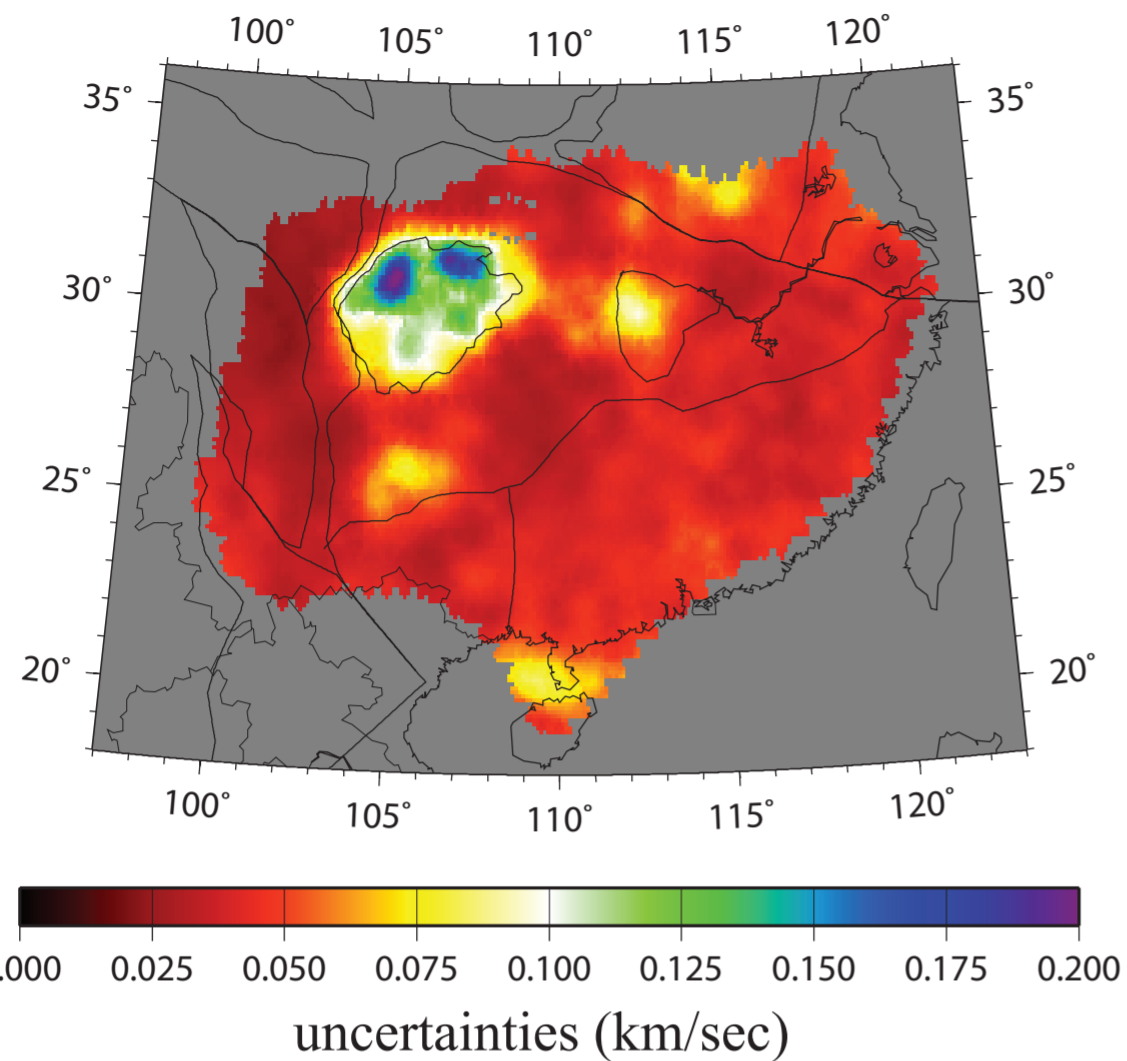
depth = 70km
4.52 km/sec
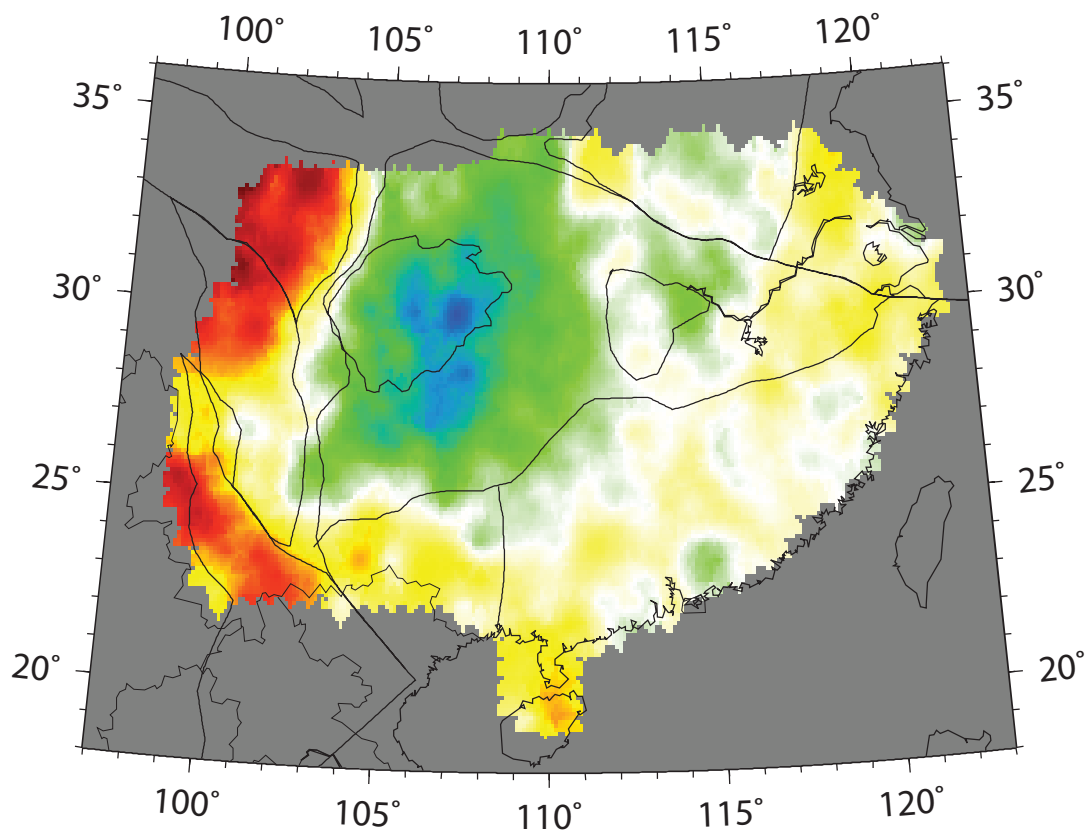
depth = 140km
4.46 km/sec

Figure 14 of 17
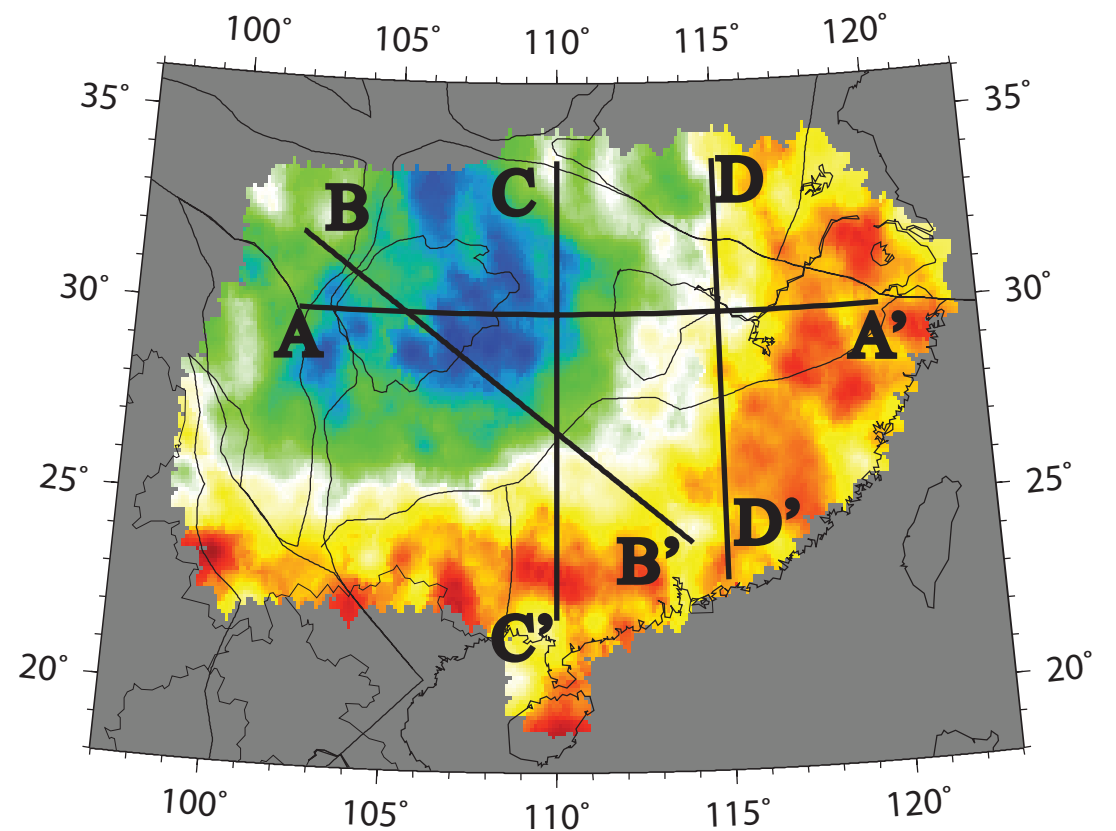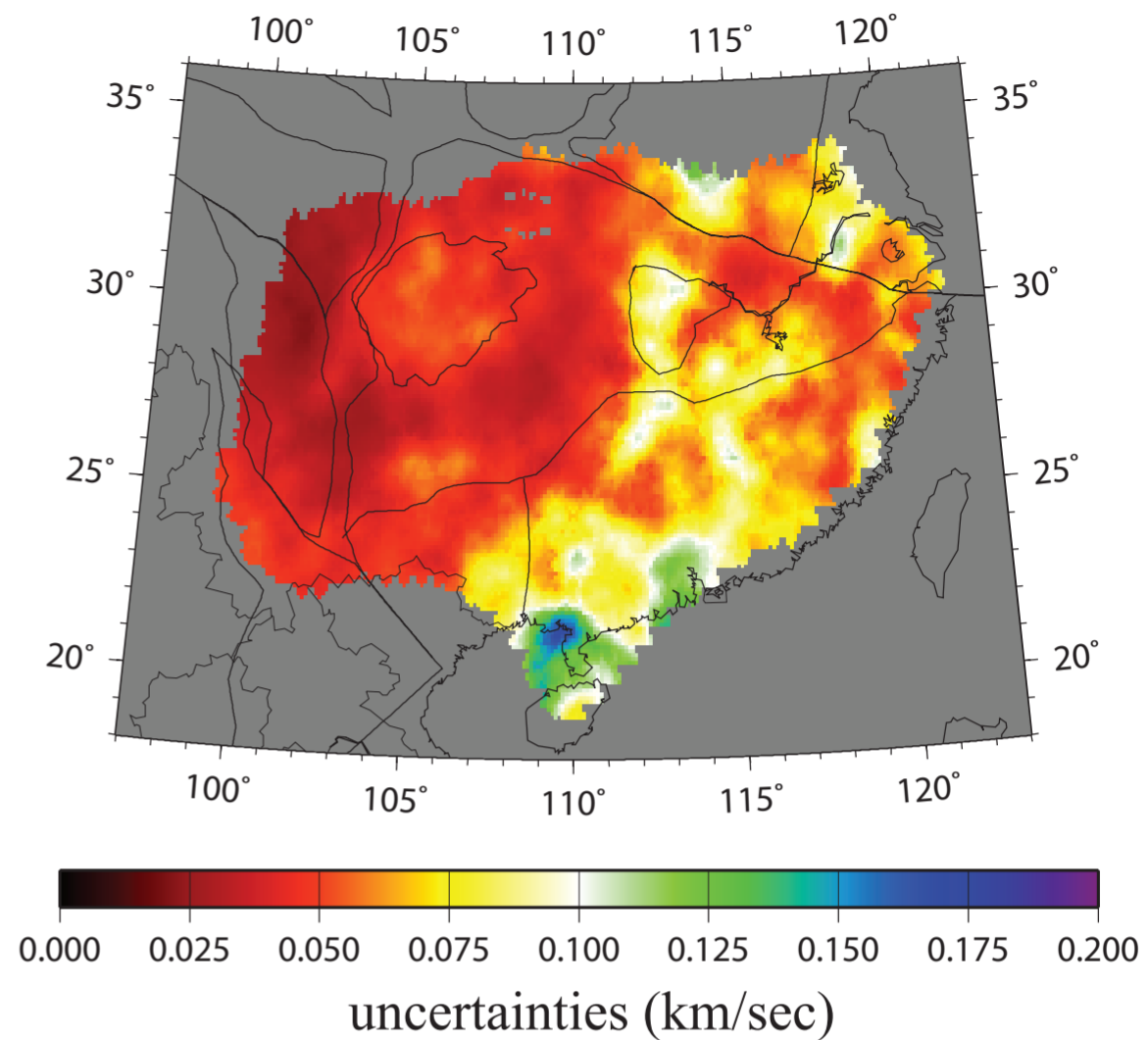
# Crustal thickness (km)
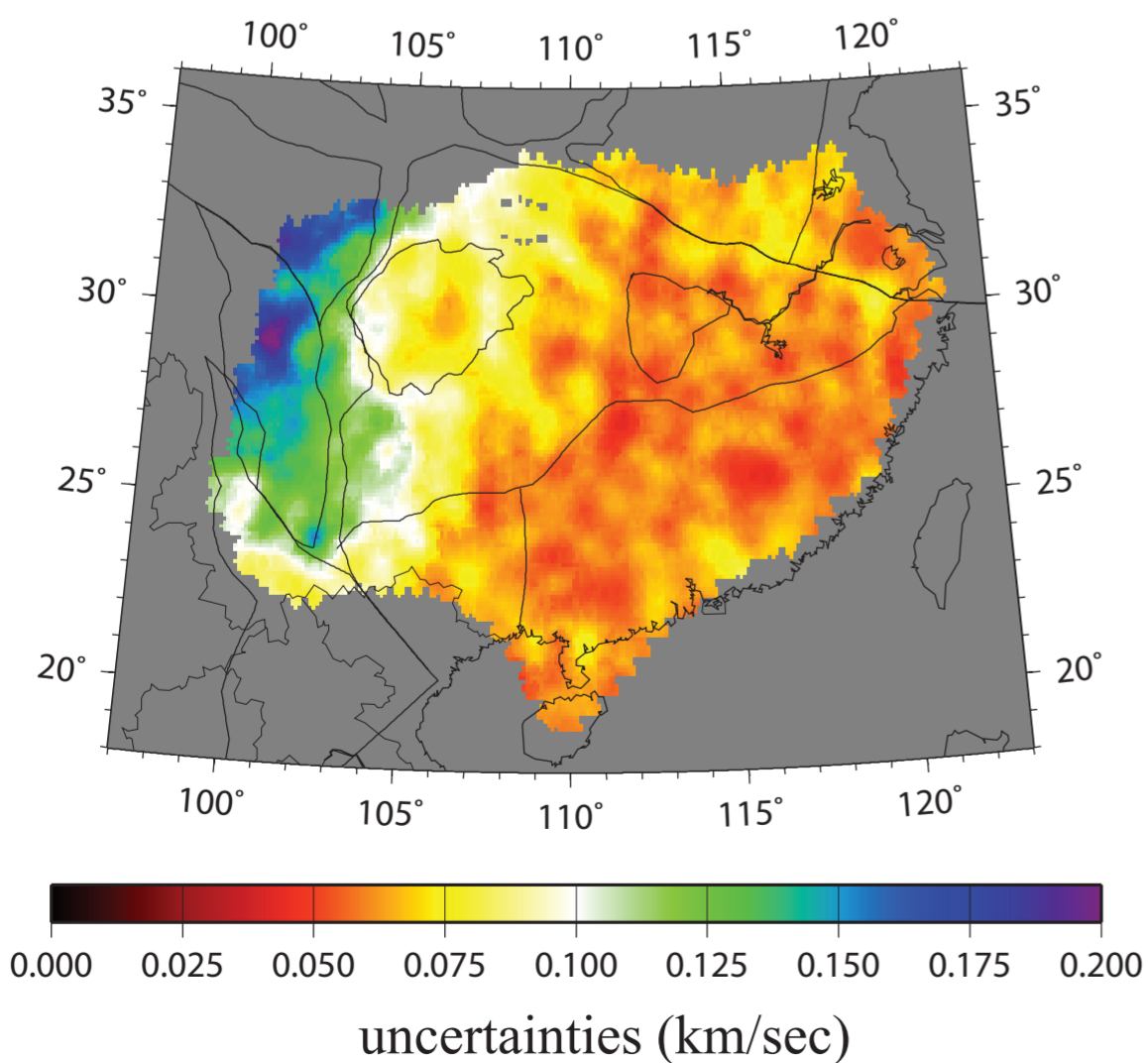
# Uncertainties (km)



Figure 15 of 17
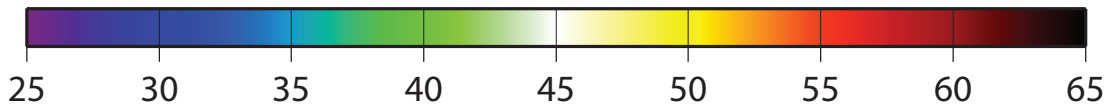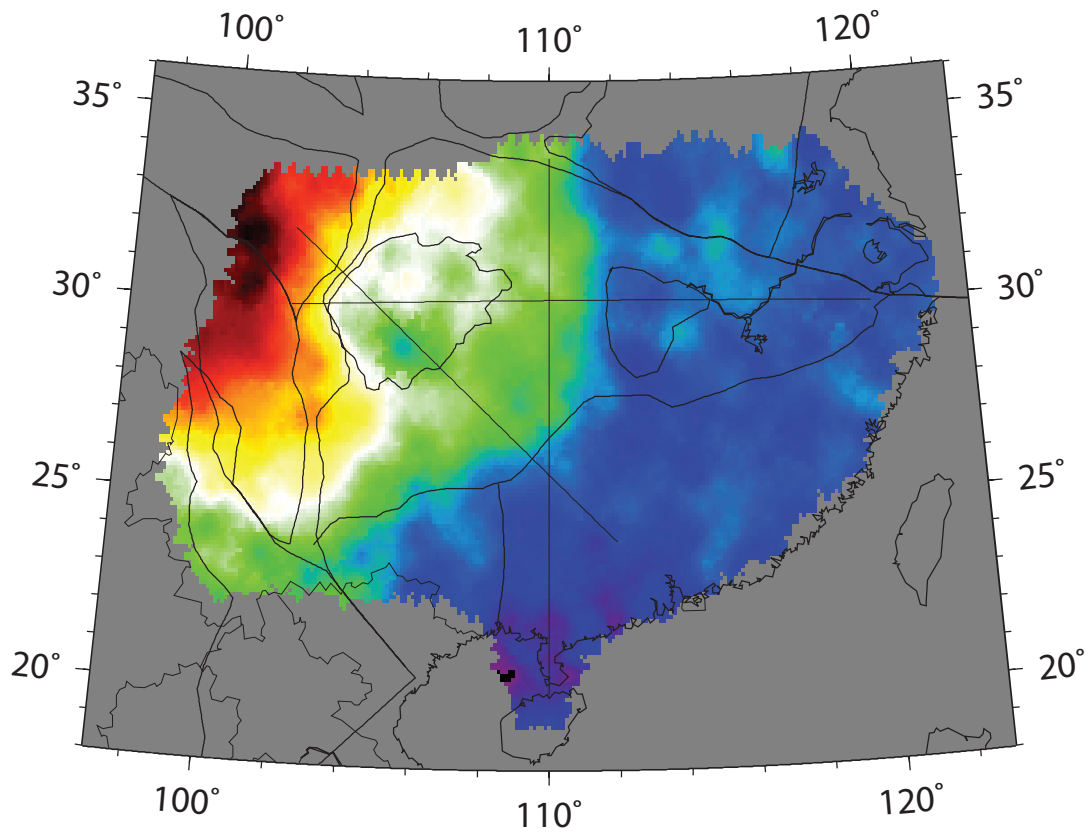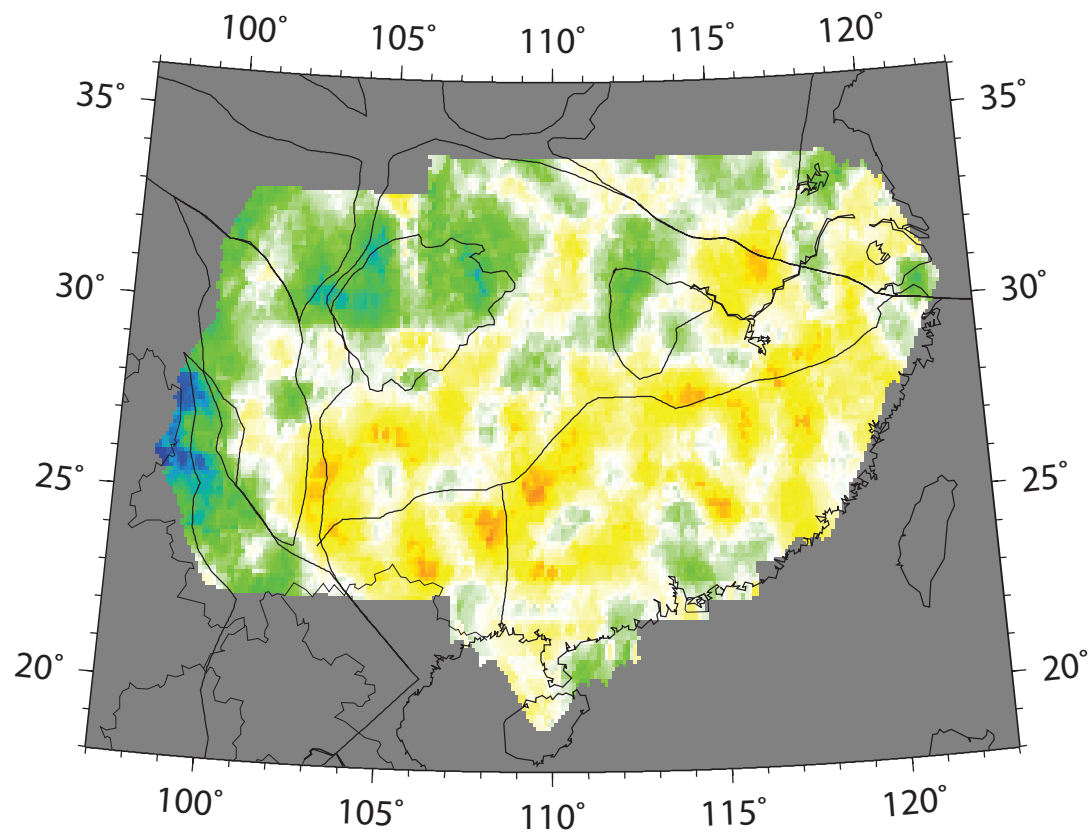
(a) depth = 10 km

(b) depth = 25 km

(c) depth = 70 km

(d) depth = 140 km

uncertainties (km/sec)

Figure 16 of 17

Figure 17 of 17